The nonlinear negative stiffness inertial amplifier base isolators for dynamic systems

Sudip Chowdhury[a,*], Arnab Banerjee[a], Sondipon Adhikari[b]

[a] *Civil Engineering Department, Indian Institute of Technology Delhi, India*
[b] *James Watt School of Engineering, The University of Glasgow, Glasgow, Scotland, UK*

Abstract

The nonlinear negative stiffness inertial amplifier base isolators (NNSIABI) for vibration reduction of dynamic systems are introduced in this paper. H_2 and H_∞ optimization methods are applied to derive the exact closed-form expressions for the optimal design parameters of novel isolators. For SDOF system, the dynamic response reduction capacity of H_2 and H_∞ optimized linear NSIABI are significantly 64.78 % and 77.14 % superior to the optimum traditional base isolators. In contrast, the dynamic response reduction capacities of H_2 and H_∞-optimized nonlinear NNSIABI are significantly 64.66 % and 66.56 % superior to the optimum traditional base isolators. For MDOF systems, the optimum linear NSIABI's dynamic response reduction capacities are significantly 95.06 % and 97.80 %, superior to the optimum traditional base isolators. In addition, the optimum nonlinear NNSIABI are significantly 94.88 % and 97.68 %, superior to the traditional base isolators. All the results are mathematically corrected and applicable for practical applications.

Keywords: Linear and nonlinear negative stiffness inertial amplifier base isolators, NSIABI, NNSIABI, Exact closed-form, H_2 and H_∞ optimization methods, SDOF and MDOF systems.

1. Introduction

The base isolation mechanisms were first invented in 1870 by Touaillon Touaillon (1870) and then applied to different structures, such as vehicle suspension Bai et al. (2017); Lindberg et al. (2014) to liquid storage tanks Abalı and Uckan (2010); Cheng et al. (2017), buildings Furinghetti et al. (2020, 2019, 2021); Mazza (2019); Sierra et al. (2019), bridges Sheng et al. (2022); Tubaldi et al. (2018), and aircraft landing gear Han et al. (2019); de Haro Moraes et al. (2018), for dynamic response mitigation of them Aly and Salem (2013); Du et al. (2011); Ebrahimi et al. (2011); Ong et al. (2017); Wei et al. (2011) subjected to the vibration. The base isolation mitigates the maximum dynamic responses of the isolated structures Ahmad et al. (2009); Hwang and Chiou (1996); Kazeminezhad et al. (2020). Apart from the linear base isolators, the nonlinear base isolators Nguyen et al. (2022), such as new zealand bearing Buckle (1985), a lead rubber bearing Robinson (1982), a resilient friction base isolator Jangid (2005a), a friction-pendulum system Jangid (2005b), a pure-friction system Shakib and Fuladgar (2003); Xi et al. (2022) are also

*Corresponding author
Email address: sudip.chowdhury@civil.iitd.ac.in (Sudip Chowdhury)

applied to the structure to control their dynamic responses Toygar et al. (2022); Zhang et al. (2019b).

The optimal system parameters, such as the isolators' natural frequency and damping ratio, must be determined before installing them to the structures. Therefore, to derive them mathematically in terms of closed-form expressions, H_2 and H_∞ optimization methods are applied. H_2 optimization methods Li et al. (2023) are applied to derive the exact closed-form expressions for the optimal design parameters of the natural frequency and damping ratio of isolators subjected to random-white noise excitations Asami et al. (2002); Baduidana and Kenfack-Jiotsa (2021); Čakmak et al. (2021); Cheng et al. (2020); Crandall and Mark (2014); Hu and Chen (2015); Palazzo and Petti (1999); Qian et al. (2019a); Roberts and Spanos (2003); Sun et al. (2019). The maximum standard deviation of the structural dynamic responses are reduced using H_2-optimized isolators. H_∞ optimization method applies for harmonic excitation to derive exact closed-form expressions for optimal design parameters of isolators Allen (2012); Cheung and Wong (2011); Chun et al. (2015); Den Hartog (1985); Hua et al. (2018). The maximum dynamic response of isolated structures are reduced using H_∞-optimized isolators Chowdhury and Banerjee (2022); Peng et al. (2021).

The dynamic response reduction capacity of isolators are increased using effective mass amplification, negative stiffness, and negative mass, and other different additionally applied mechanical metamaterial devices Ayad et al. (2020a); Čakmak et al. (2022); Chen and Hu (2019); De Domenico et al. (2019); Jiang et al. (2020); Kuhnert et al. (2020); Moghimi and Makris (2020); Qian et al. (2019b); Smith and Wang (2004); Wang et al. (2009); Zhang et al. (2019a, 2018); Zhao et al. (2019, 2020a,b). The inerters and inertial amplifiers are one of the effective mass amplification devices where large band-gap find out at low frequencies Ayad et al. (2020b); Barys et al. (2018); Barys and Zalewski (2018); Chowdhury et al. (0, 2021, 2022); Frandsen et al. (2016); Hou et al. (2017); Karathanasopoulos et al. (2020); Miniaci et al. (2020); Muhammad et al. (2020); Sun et al. (2021); Taniker and Yilmaz (2013, 2017); Yilmaz and Hulbert (2010, 2017); Yilmaz et al. (2007); Yilmaz (2007); Yuksel and Yilmaz (2015); Zhou et al. (2019). Quasi-zero stiffness Carrella et al. (2009, 2007); Hao and Cao (2015); Li et al. (2021); Robertson et al. (2009); Zhao et al. (2021), high-static-low-dynamic stiffness Cheng et al. (2016); Wu et al. (2022); Zheng et al. (2016), and Euler buckled beams as negative stiffness elements Fulcher et al. (2014); Huang et al. (2014); Liu et al. (2013); Winterflood et al. (2002); Yuan et al. (2021), pseudo-negative-stiffness Iemura et al. (2006); Iemura and Pradono (2009); Kapasakalis et al. (2020, 2021); Wang et al. (2018), negative-stiffness inclusions Lakes et al. (2001), magnetic negative stiffness dampers Shi and Zhu (2017); Wu et al. (2014) are one of the negative stiffness devices. A negative stiffness device (NSD) that can simulate the structural system's weakening without causing permanent deformations or inelastic excursions. By engaging at a predetermined displacement and exerting a force at the installation level that resists the structural restoring force, the NSD mimics yielding Sarlis et al. (2013). The NSD comprises a gap spring assembly (GSA) mechanism that postpones the engagement of negative stiffness until the structural system experiences a predetermined displacement and a self-contained highly compressed spring in a double negative stiffness magnification mechanism Pasala et al. (2013). The significant vertical forces required for the formation of the horizontal negative stiffness are self-contained by the NSD's double chevron bracing, which prevents the forces from being transferred to the structure Sarlis et al. (2016). A negative stiffness amplifying damper (NSAD) is also developed by integrating a negative stiffness (NS) spring into the viscous damper systems that are flexible and supported by a standard Maxwell damping element (MDE) Wang et al. (2019b). When the NS spring and MDE's dashboard are coupled, the stroke of the dashboard is amplified, which results in a notable dampening Wang et al. (2019a) and amplified effect. In addition to producing a notable damping and magnifying effect, the suggested NSAD also maintains the negative stiffness characteristic Wang et al. (2022). When an earthquake occurs, this characteristic is appealing since it lessens both displacement and structural acceleration Wang et al. (2023). However, the linear and nonlinear negative stiffness inertial amplifier base isolators are not introduced in any state of the art. A research scope has been found out.

Therefore, the linear and nonlinear negative stiffness inertial amplifier base isolators, such as NSIABI and NNSIABI, for dynamic response mitigation of single-degree-of-freedom and multi-degree-of-freedom systems are introduced in this paper. H_2 and H_∞ optimization methods are applied to derive the exact closed-form expressions for the optimal design parameters of the novel isolators, such as the natural frequency and damping ratio of the isolator. The dynamic response reduction capacity of H_2 and H_∞-optimized NSIABI and NNSIABI are determined with respect to the dynamic response reduction capacity of optimum traditional base isolators for SDOF and MDOF systems subjected to harmonic and random-white noise excitation.

2. Structural model and equations of motion

The structural model of a single degree of freedom system (SDOF) isolated by negative stiffness inertial amplifier base isolator (NSIABI) subjected to base excitation has been shown in Figure 1. m_b, k_b, and c_b define the static mass, static stiffness, and static damp-

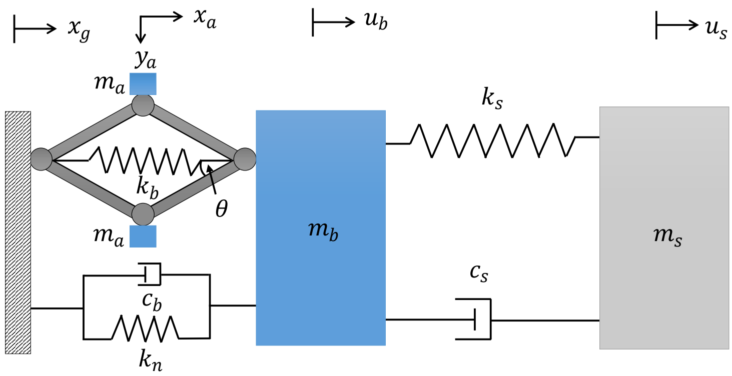

Figure 1: The structural diagram of a single degree of freedom system isolated by negative stiffness inertial amplifier base isolator subjected to base excitation.

ing of NSIABI without considering the effective mass amplification effect of the inertial amplifiers. m_a and θ define the amplifier mass and inertial angle. k_n defines the negative stiffness installed inside the core of the base isolator. $\ddot{x}_g$ defines the base excitation. m_s, c_s, and k_s define the mass, damping, and stiffness of the SDOF system. A small amplitude vibration applies at the base of this above-showed isolated structure. Therefore, a small deflection generates through the amplifier mass m_a in x and y directions, i.e., x_a and y_a.

Therefore, the deflections are derived as

$$x_a = \frac{u_b + x_g}{2} \quad \text{and} \quad y_a = \pm\frac{u_b - x_g}{2\tan\theta} \tag{1}$$

A certain amount of inertial force is also generated through the amplifier mass in x and y directions due to the deflection, i.e., v_x and v_y. Hence, the inertial forces are derived as

$$v_x = m_a \ddot{x}_a \quad \text{and} \quad v_y = m_a \ddot{y}_a \tag{2}$$

Some amount of inertial forces is also developed through the rigid links connected by the amplifier mass, i.e., v_1 and v_2. Accordingly, p_1 and p_2 are derived as

$$v_1 = \frac{1}{2}\left(\frac{v_y}{\sin\theta} - \frac{v_x}{\cos\theta}\right) \quad \text{and} \quad v_2 = \frac{1}{2}\left(\frac{v_y}{\sin\theta} + \frac{v_x}{\cos\theta}\right) \tag{3}$$

The resultant force of all inertial forces is generated from the end terminal of the inertial amplifier, which is connected by the isolator mass and base of the isolated structure. Therefore, the resultant force is derived as

$$\begin{aligned} V &= 2v_2\cos\theta + k_b(u_b - x_g) \\ &= \underbrace{\frac{0.5m_a}{\tan^2\theta}}_{w_1}(\ddot{u}_b - \ddot{x}_g) + \underbrace{0.5m_a}_{w_2}(\ddot{u}_b + \ddot{x}_g) + k_{ia}(u_b - x_g) \end{aligned} \tag{4}$$

where $w_1 = (0.5m_a/\tan^2\theta)$ and $w_2 = 0.5m_a$ are the additional amplified masses which are added to the static mass of the isolator to generate the effective mass for NSIABI. Therefore, the effective mass of NSIABI derives as

$$m_{ia} = m_b + 0.5m_a\left(1 + \frac{1}{\tan^2\theta}\right) \tag{5}$$

Applying this effective mass, the other governing system parameters, such as effective stiffness and effective damping are derived as

$$k_{ia} = m_{ia}\omega_b^2 \quad \text{and} \quad c_{ia} = 2\zeta_b m_{ia}\omega_b \tag{6}$$

Newton's second law applies to derive the governing equations of motion for the SDOF system isolated by NSIABI subjected to base excitation and expressed as

$$\begin{aligned} m_{ia}\ddot{x}_b + c_{ia}\dot{x}_b + (k_{ia} - k_n)\,x_b - k_s x_s - c_s\dot{x}_s &= -m_{ia}\ddot{x}_g \\ m_s\ddot{x}_s + m_s\ddot{x}_b + c_s\dot{x}_s + k_s x_s &= -m_s\ddot{x}_g \end{aligned} \tag{7}$$

where $x_b = u_b - x_g$ defines the relative dynamic response of NSIABI w.r.t the base, $x_s = u_s - u_b$ defines the relative dynamic response of the SDOF system w.r.t isolator. The steady-state solutions for the dynamic responses of the isolated structures consider $x_s = X_s e^{\mathrm{i}\omega t}$, $x_b = X_b e^{\mathrm{i}\omega t}$, and $\ddot{x}_g = X_g e^{\mathrm{i}\omega t}$. $\zeta_b = \frac{c_{ia}}{2\omega_b m_{ia}}$ defines damping ratio, and $\omega_b = \sqrt{k_{ia}/m_{ia}}$ defines the frequency ratio for NSIABI. $\mu_b = m_b/m_s$ defines base mass ratio, i.e., isolator to main structural mass ratio. $\mu_{ia} = m_{ia}/m_s$ defines effective base mass ratio, i.e., isolator effective to main structural mass ratio. $\beta = k_n/k_{ia}$ defines the ratio of effective negative stiffness to isolator effective stiffness. $\eta_b = \omega_b/\omega_s$ defines the natural frequency ratio of the isolator to the main structure. $\mu_a = m_a/m_s$ defines the amplifier mass ratio, i.e., amplifier mass to main structural mass ratio. $\zeta_s = \frac{c_s}{2 m_s \omega_s}$ and $k_s = m_s \omega_s^2$ define the damping ratio and stiffness of the main structure. Therefore, using these system parameters and steady-state solutions to the equations of motion, a transfer function derives from determining the dynamic responses of the main structure and NSIABI analytically. Therefore, the transfer function derives as

$$\begin{gathered} \begin{bmatrix} 2\,\zeta_s q \omega_s + q^2 + {\omega_s}^2 & q^2 \\ -2\,\zeta_s q \omega_s - {\omega_s}^2 & B_{22} \end{bmatrix} \begin{Bmatrix} X_s \\ X_b \end{Bmatrix} = - \begin{bmatrix} 1 \\ \mu_{ia} \end{bmatrix} X_g \\ B_{22} = -\beta\,\mu_{ia} {\omega_b}^2 + 2\,\zeta_b q \omega_b \mu_{ia} + \mu_{ia} q^2 + {\omega_b}^2 \mu_{ia} \end{gathered} \tag{8}$$

The dynamic response of the main structure has been derived as

$$H_s(q) = \frac{X_s}{X_g} = \frac{-\omega_b \left(\omega_b \beta - 2\,\zeta_b q - \omega_b\right) \mu_{ia}}{\Delta} \tag{9}$$

The dynamic response of NSIABI has been derived as

$$H_b(q) = \frac{X_b}{X_g} = \frac{\begin{array}{c} -2\,q \zeta_s \mu_{ia} \omega_s - \mu_{ia} q^2 - 2\,\zeta_s q \omega_s \\ -\mu_{ia} {\omega_s}^2 - {\omega_s}^2 \end{array}}{\Delta} \tag{10}$$

Δ derives as

$$\Delta = \begin{array}{c} q^4 \mu_{ia} \\ + \left(\; 2\,\zeta_b \mu_{ia} \omega_b + 2\,\zeta_s \mu_{ia} \omega_s + 2\,\zeta_s \omega_s \; \right) q^3 \\ + \left(\begin{array}{c} 4\,\zeta_b \zeta_s \mu_{ia} \omega_b \omega_s - \beta\,\mu_{ia} {\omega_b}^2 + {\omega_s}^2 \\ + \mu_{ia} {\omega_b}^2 + \mu_{ia} {\omega_s}^2 \end{array} \right) q^2 \\ + \left(\begin{array}{c} -2\,\beta\,\zeta_s \mu_{ia} {\omega_b}^2 \omega_s + 2\,\zeta_b \mu_{ia} \omega_b {\omega_s}^2 \\ + 2\,\zeta_s \mu_{ia} {\omega_b}^2 \omega_s \end{array} \right) q \\ -\beta\,\mu_{ia} {\omega_b}^2 {\omega_s}^2 + \mu_{ia} {\omega_b}^2 {\omega_s}^2 \end{array} \tag{11}$$

2.1. H_2 optimization for white-noise random excitation

H_2 optimization method applies to derive the exact closed-form expression for optimal design parameters of NSIABI subjected to white-noise excitation Chowdhury et al. (2022). Equation (11) is a 4^{th} order polynomial equation. Therefore, considering the order of the polynomials, a formulation derives and expressed as

$$\sigma^2_{x_{s,b}} = \int_{-\infty}^{\infty} \frac{\Xi_n(\omega)\,\mathrm{d}\omega}{\Lambda_n(\mathrm{i}\omega)\Lambda_n^*(\mathrm{i}\omega)} = \frac{\pi}{u_4} \frac{\det[\mathbf{N}_4]}{\det[\mathbf{D}_4]} \tag{12}$$

$$N_4 = \begin{bmatrix} v_3 & v_2 & v_1 & v_0 \\ -u_4 & u_2 & -u_0 & 0 \\ 0 & -u_3 & u_1 & 0 \\ 0 & u_4 & -u_2 & u_0 \end{bmatrix} \quad \text{and} \quad D_4 = \begin{bmatrix} u_3 & -u_1 & 0 & 0 \\ -u_4 & u_2 & -u_0 & 0 \\ 0 & -u_3 & u_1 & 0 \\ 0 & u_4 & -u_2 & u_0 \end{bmatrix} \tag{13}$$

Equation (9) and Eq. (11) are substituted in Eq. (12) and Eq. (13). Hence, the standard deviation (SD) of the dynamic response of the main structure derives as

$$\sigma_{x_s}^2 = \frac{S_0 \pi\, \omega_b \left(\mu_{ia} {\omega_b}^2 \beta^2 + 4\, {\zeta_b}^2 \mu_{ia} {\omega_s}^2 - 2\, \beta\, \mu_{ia} {\omega_b}^2 - \beta\, {\omega_s}^2 + \mu_{ia} {\omega_b}^2 + {\omega_s}^2\right)}{2 \zeta_b {\omega_s}^6} \tag{14}$$

Equation (14) partially differentiates w.r.t damping ratio and natural frequency of NSIABI. Therefore, a mathematical formulation for partial differentiation derives as

$$\frac{\partial \sigma_{x_s}^2}{\partial \zeta_b} = 0 \quad \text{and} \quad \frac{\partial \sigma_{x_s}^2}{\partial \omega_b} = 0 \tag{15}$$

Equation (14) substitutes in the first equation of Eq. (15). Accordingly, the damping ratio of NSIABI derives as

$$\zeta_b = \frac{\sqrt{\mu_{ia} \left(\mu_{ia} {\omega_b}^2 \beta^2 - 2\, \beta\, \mu_{ia} {\omega_b}^2 - \beta\, {\omega_s}^2 + \mu_{ia} {\omega_b}^2 + {\omega_s}^2\right)}}{2 \mu_{ia} \omega_s} \tag{16}$$

Equation (16) substitutes further in Eq. (14) to derive the optimal closed-form solution for the natural frequency of NSIABI. Therefore, the upgraded standard deviation of the dynamic response of the main structure derives as

$$\sigma_{x_s}^2 = \frac{2 \omega_b S_0 \left(\beta - 1\right) \mu_{ia} \left({\omega_b}^2 \left(\beta - 1\right) \mu_{ia} - {\omega_s}^2\right) \pi}{\sqrt{\mu_{ia} \left({\omega_b}^2 \left(\beta - 1\right) \mu_{ia} - {\omega_s}^2\right) \left(\beta - 1\right)} {\omega_s}^5} \tag{17}$$

The exact closed-form expression for the optimal natural frequency of NSIBAI derives as

$$(\omega_b)_{\text{opt}} = \frac{\omega_s}{\sqrt{2\, \mu_{ia} - 2\, \beta\, \mu_{ia}}} \quad \text{and} \quad (\omega_b)_{\text{opt}} = \frac{\omega_s}{\sqrt{\left(2 - 2\, \beta\right) \left(\mu_b + 0.5 \mu_a \left(1 + \frac{1}{\tan^2 \theta}\right)\right)}} \tag{18}$$

Equation (18) substitutes in Eq. (16) and Eq. (17) to derive the optimal closed-form solution for the optimal damping ratio of NSIABI and SD of the dynamic response of the main structure. Accordingly, the exact closed-form expression for optimal damping ratio of NSIABI has been derived as

$$(\zeta_b)_{\text{opt}} = \sqrt{\frac{1 - \beta}{8 \mu_{ia}}} \quad \text{and} \quad (\zeta_b)_{\text{opt}} = \sqrt{\frac{1 - \beta}{8 \left(\mu_b + 0.5 \mu_a \left(1 + \frac{1}{\tan^2 \theta}\right)\right)}} \tag{19}$$

The variations of the optimal frequency ratio of NSIABI versus base mass ratio for different values of amplifier mass ratio are displayed in Figure 2 (a). For an increment of base mass and amplifier mass ratios, the frequency ratio of the isolator decreases. The systems parameters are taken for this graph $\theta = 10^o$ and $\beta = 0.10$. In contrast, the optimal frequency ratio increases when the inertial angle increases, which shows in Figure 2 (b). Therefore, for a flexible base with a sufficient load-bearing capacity, a moderate base mass ratio, amplifier mass ratio, and inertial angle are recommended. The variations of the optimal damping ratio of the isolator versus base mass ratio are displayed in Figure 3 (a). For higher values of base mass ratio and amplifier mass ratio, the optimal damping ratio of the isolator decreases. In contrast, the isolator damping ratio increases when the inertial angle increases, as shown in Figure 3 (b). Therefore, a moderate damping ratio for NSIABI achieves using a moderate base mass ratio, a moderate amplifier mass ratio, and a higher inertial angle.

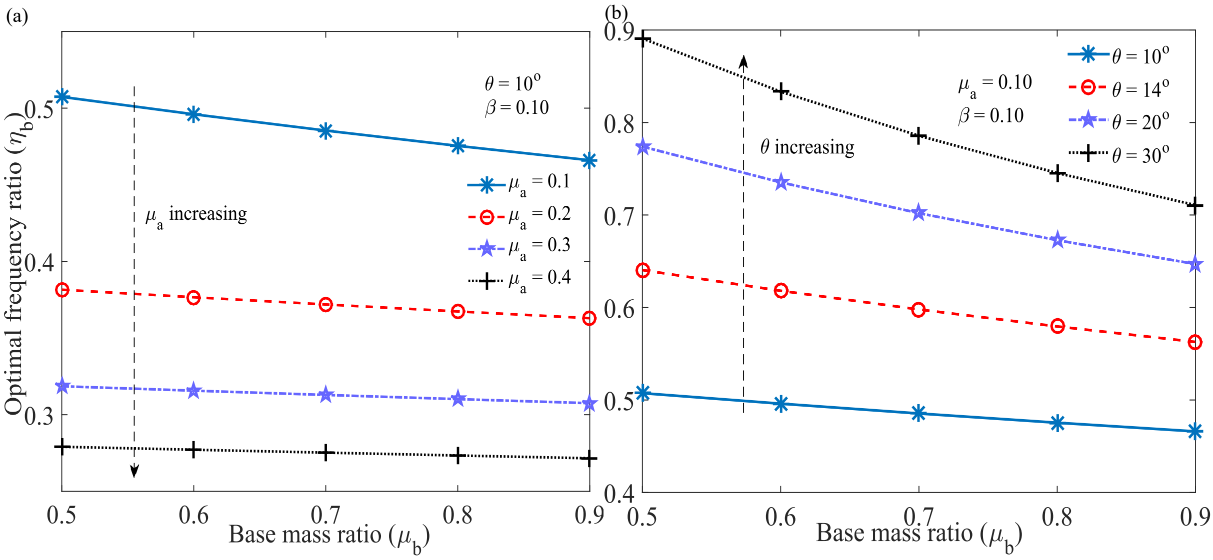

Figure 2: The variations of optimal frequency ratio of NSIABI versus base mass ratio for different values of (a) amplifier's mass ratio and (b) inertial angle.

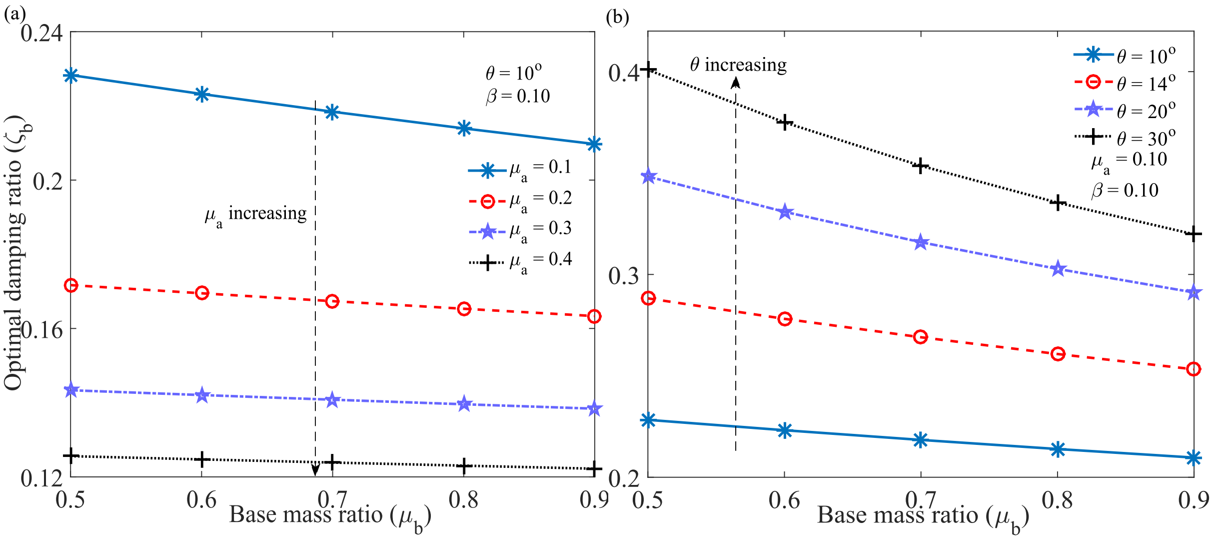

Figure 3: The variations of optimal damping ratio of NSIABI versus base mass ratio for different values of (a) amplifier's mass ratio and (b) inertial angle.

2.2. H_∞ optimization for harmonic excitation

H_∞ optimization method has been performed to minimize the maximum displacement of the isolated multi-storey building subjected to harmonic excitation. It has been applied for this paper to derive the analytical closed-form expressions for optimal design parameters of IABI for vibration mitigation of multi-storey buildings, respectively Chowdhury et al. (2022). To perform that Eq. (66) has been transformed into a non-dimensional form. Therefore, the non-dimensional displacement response has been derived as

$$\begin{bmatrix} -\eta^2 + 2\,\mathrm{i}\zeta_s\eta + 1 & -\eta^2 \\ -1 & B_{22} \end{bmatrix} \begin{Bmatrix} X_s \\ X_b \end{Bmatrix} = -\begin{bmatrix} 1 \\ \mu_{ia} \end{bmatrix} \frac{X_g}{\omega_s^2} \tag{20}$$
$$B_{22} = -\mu_{ia}\eta^2 + 2\,\mathrm{i}\zeta_b\eta\,\eta_b\mu_{ia} - \beta\,{\eta_b}^2\mu_{ia} + {\eta_b}^2\mu_{ia}$$

The dynamic response of the main structure has been derived as

$$H_s(\eta) = \left(\frac{X_s}{X_g}\right)\omega_s^2 = \frac{\eta_b\left(2\,\mathrm{i}\eta\,\zeta_b - \beta\,\eta_b + \eta_b\right)\mu_{ia}}{\Delta} \tag{21}$$

The dynamic response of NSIABI derives as

$$H_s(\eta) = \left(\frac{X_b}{X_g}\right)\omega_s^2 = \frac{-\mu_{ia}\eta^2 + \mu_{ia} + 1 + \mathrm{i}\left(2\,\mu_{ia}\zeta_s\eta + 2\,\zeta_s\eta\right)}{\Delta} \tag{22}$$

Δ derives as

$$\Delta = \begin{array}{c} -\beta\,\eta^2{\eta_b}^2\mu_{ia} + 4\,\eta^2\zeta_b\zeta_s\eta_b\mu_{ia} - \eta^4\mu_{ia} + \eta^2{\eta_b}^2\mu_{ia} \\ +\beta\,{\eta_b}^2\mu_{ia} + \mu_{ia}\eta^2 - {\eta_b}^2\mu_{ia} + \eta^2 \\ +\mathrm{i}\left(\begin{array}{c} 2\,\beta\,\eta\,\zeta_s{\eta_b}^2\mu_{ia} + 2\,\eta^3\zeta_b\eta_b\mu_{ia} + 2\,\eta^3\zeta_s\mu_{ia} \\ -2\,{\eta_b}^2\zeta_s\mu_{ia}\eta + 2\,\eta^3\zeta_s - 2\,\zeta_b\eta\,\eta_b\mu_{ia} \end{array}\right) \end{array} \tag{23}$$

where $\eta = \omega/\omega_s$ defines the frequency ratio of excitation to the main structure. Hence, to minimize the maximum dynamic response of the main structure, the fixed-point theory/H_∞ optimization method applies. To apply H_∞ optimization method, the modulus of $H_s(\eta)$ derives and expresses as

$$|H_s(\eta)| = \sqrt{\frac{A^2 + \zeta_b^2 B^2}{C^2 + \zeta_b^2 D^2}} = \left|\frac{B}{D}\right| \sqrt{\frac{\left(\frac{A}{B}\right)^2 + \zeta_b^2}{\left(\frac{C}{D}\right)^2 + \zeta_b^2}} \tag{24}$$

$$\begin{aligned} A &= -\beta\,{\eta_b}^2\mu_{ia} + {\eta_b}^2\mu_{ia} \\ B &= 2\eta\,\eta_b\mu_{ia} \\ C &= -\beta\,\eta^2{\eta_b}^2\mu_{ia} - \eta^4\mu_{ia} + \eta^2{\eta_b}^2\mu_{ia} + \beta\,{\eta_b}^2\mu_{ia} + \mu_{ia}\eta^2 - {\eta_b}^2\mu_{ia} + \eta^2 \\ D &= 2\,\eta\,\eta_b\mu_{ia}\left(\eta^2 - 1\right) \end{aligned} \tag{25}$$

Two constraints have been applied to derive the optimal frequency, and damping ratio of the main structure using the fixed point theory Chowdhury et al. (2022); Den Hartog (1985). These constraints are listed below.

$$\left.\left(\frac{A}{B}\right)^2\right|_{\eta_j} = \left.\left(\frac{C}{D}\right)^2\right|_{\eta_j} \quad \text{and} \quad \left.\left(\frac{B}{D}\right)^2\right|_{\eta_1} = \left.\left(\frac{B}{D}\right)^2\right|_{\eta_2} \tag{26}$$

Now applying the first constraint, the values of $\eta_{1,2}$ have been obtained as Chowdhury et al. (2022)

$$\eta^4\mu_{ia} + \left(2\,\beta\,{\eta_b}^2\mu_{ia} - 2\,{\eta_b}^2\mu_{ia} - \mu_{ia} - 1\right)\eta^2 - 2\,\beta\,{\eta_b}^2\mu_{ia} + 2\,{\eta_b}^2\mu_{ia} = 0 \tag{27}$$

Now applying the second constraint, the values of $\eta_{1,2}$ have been obtained as

$$\eta_1^2 + \eta_2^2 = 2 \tag{28}$$

From Eq. (27), the relation between two roots has been derived and expressed as

$$\eta_1^2 + \eta_2^2 = \frac{-2\,\beta\,{\eta_b}^2 \mu_{ia} + 2\,{\eta_b}^2 \mu_{ia} + \mu_{ia} + 1}{\mu_{ia}} \tag{29}$$

After equating Eq. (28) and Eq. (29), the optimal frequency ratio of NSIABI has been derived as

$$(\eta_b)_{\mathrm{opt}} = \sqrt{\frac{\mu_{ia} - 1}{2\mu_{ia}\,(1-\beta)}} \quad \text{and} \quad (\eta_b)_{\mathrm{opt}} = \sqrt{\frac{\left(\mu_b + 0.5\mu_a\left(1 + \frac{1}{\tan^2\theta}\right)\right) - 1}{2\left(\mu_b + 0.5\mu_a\left(1 + \frac{1}{\tan^2\theta}\right)\right)(1-\beta)}} \tag{30}$$

$\eta_{1,2}^2$ has been derived as

$$(\eta_{1,2})^2_{\mathrm{opt}} = 1 \pm \sqrt{\frac{1}{\mu_{ia}}} \tag{31}$$

The optimal damping ratio of NSIABI has been derived as

$$(\zeta_b)_{\mathrm{opt}} = \sqrt{\frac{\mu_{ia} - 1 - \beta\,\mu_{ia} + \beta}{8\,\mu_{ia}}} \tag{32}$$

The variations of the optimal frequency ratio of NSIABI versus base mass ratio for different values of amplifier mass ratio are displayed in Figure 4 (a). For an increment of base mass and amplifier mass ratios, the frequency ratio of the isolator increases. The systems parameters are taken for this graph $\theta = 10^o$ and $\beta = 0.10$. In contrast, the optimal frequency ratio decreases when the inertial angle increases, which shows in Figure 4 (b). Therefore, for a flexible base with a sufficient load-bearing capacity, a moderate base mass ratio, amplifier mass ratio, and inertial angle are recommended. The variations of the optimal damping ratio of the isolator versus base mass ratio are displayed in Figure 5 (a). For higher values of base mass ratio and amplifier mass ratio, the optimal damping ratio of the isolator increases. In contrast, the isolator damping ratio decreases when the inertial angle increases, as shown in Figure 5 (b). Therefore, a moderate damping ratio for NSIABI achieves using a moderate base mass ratio, a moderate amplifier mass ratio, and a higher inertial angle.

3. Dynamic response evaluation

The optimal dynamic response of the H_2-optimized isolated structure versus frequency ratio is displayed in Figure 6 (a). The system parameters are considered as $\mu_b = 0.7$, $\mu_a = 0.1$, $\theta = 30^o$, and $\beta = 0.1$. Equation (18) and Eq. (19) apply for this graph and applying the considered system parameters, the optimal values for frequency and damping ratio determine as 0.7857 and 0.3536. The isolated structures vibrate at their Eigen frequencies for $\zeta_b = 0$, i.e., $\eta = 0.4773$ and $\eta = 1.562$. Eigen-frequencies are shifted due to resonance, and the dynamic responses are mitigated for $(\zeta_b)_{\mathrm{opt}} = 0.3536$. Therefore, optimal dynamic responses have been achieved, and the resonating frequencies

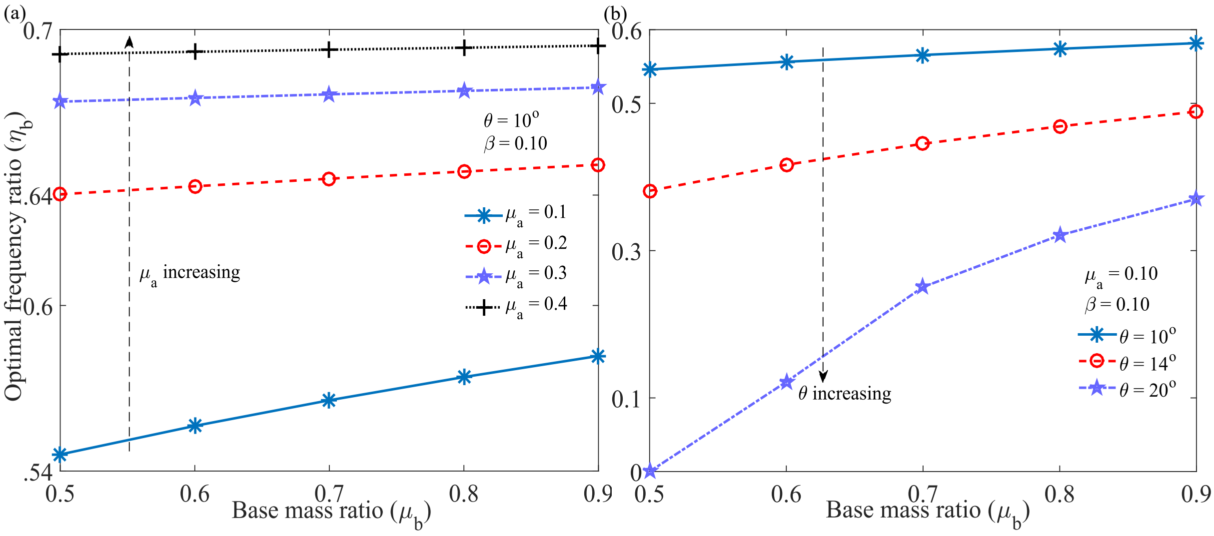

Figure 4: The variations of optimal frequency ratio of NSIABI versus base mass ratio for different values of (a) amplifier mass ratio and (b) inertial angle.

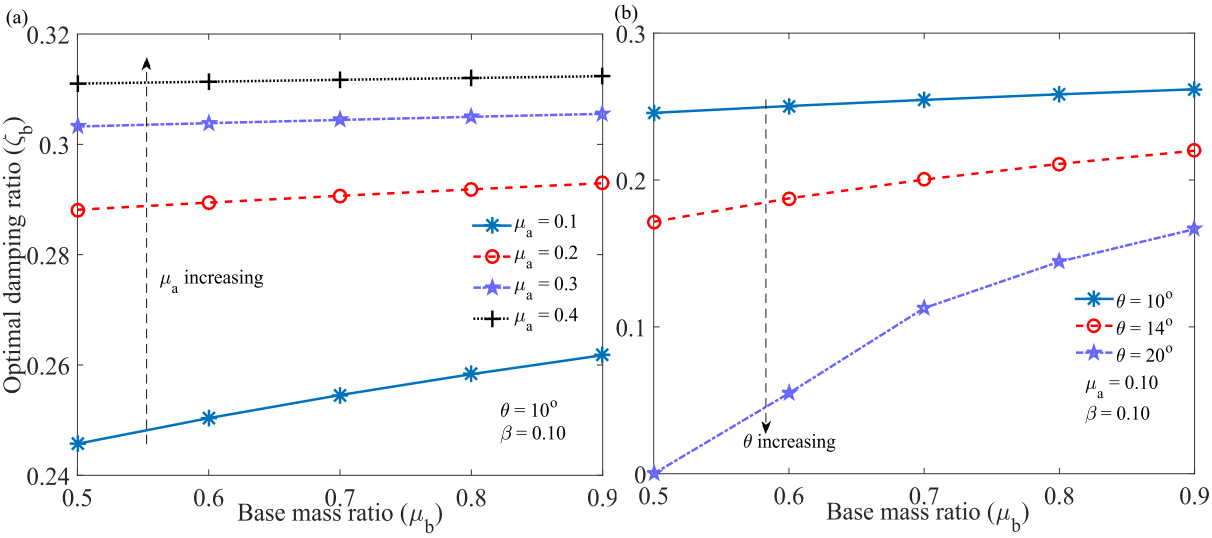

Figure 5: The variations of optimal damping ratio of NSIABI versus base mass ratio for different values of (a) amplifier's mass ratio and (b) inertial angle.

are obtained as $\eta = 0.4713$ and $\eta = 1.477$. The optimal dynamic response determines as 3.0. All the response peaks are merged into one, and the entire isolated structure vibrates as an SDOF system for $\zeta_b = \infty$. The frequency region is identified as $\eta = 1.0$. The optimal dynamic response of the H_∞-optimized isolated structure versus frequency ratio is displayed in Figure 6 (b). The system parameters are considered as $\mu_b = 0.7$, $\mu_a = 0.1$, $\theta = 14^o$, and $\beta = 0.1$. Equation (30) and Eq. (32) apply for this graph and applying the considered system parameters, the optimal values for frequency and damping ratio determine as 0.4451 and 0.2. The isolated structures vibrate at their Eigen frequencies for $\zeta_b = 0$, i.e., $\eta = 0.3222$ and $\eta = 1.311$. Eigen-frequencies are shifted due to resonance,

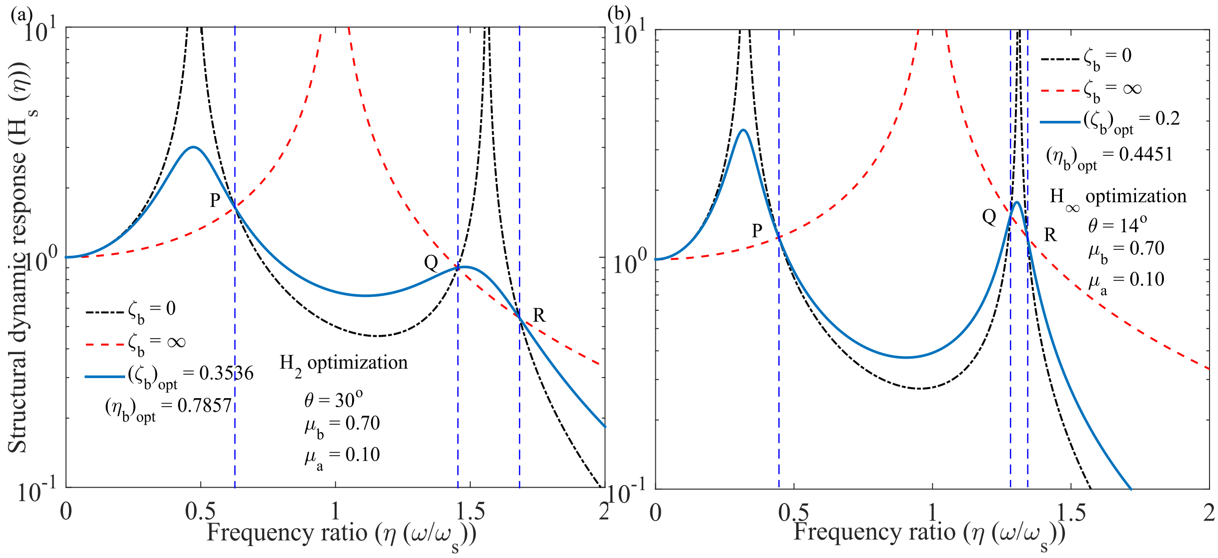

Figure 6: The optimal dynamic responses of structures vs frequency ratio isolated by (a) H_2 optimized and (b) H_∞ optimized NSIABI.

and the dynamic responses are mitigated for $(\zeta_b)_{\text{opt}} = 0.2$. Therefore, optimal dynamic responses have been achieved, and the resonating frequencies are obtained as $\eta = 0.3165$ and $\eta = 1.304$. The optimal dynamic response determines as 3.6588. All the response peaks are merged into one, and the entire isolated structure vibrates as an SDOF system for $\zeta_b = \infty$. The frequency region is identified as $\eta = 1.0$. The variations of the optimal dynamic responses of structures versus frequency ratio isolated by H_2 optimized NSIABI and traditional base isolator (TBI) subjected to harmonic excitation are shown in Figure 7 (a). For NSIABI, the system parameters are considered as $\mu_b = 0.7$, $\mu_a = 0.1$, $\theta = 30^o$, $\beta = 0.1$, $\eta_b = 0.7857$, and $\zeta_b = 0.3536$. For traditional base isolator Jangid (2007); Matsagar and Jangid (2003, 2004), the system parameters are considered as $\mu_b = 0.9$, $\zeta_b = 0.1$, and $T_b = 2$ sec, and $\eta_b = 0.5$. The main structural damping ratio considers as $\zeta_s = 0.01$. The maximum dynamic response of the uncontrolled structure obtains as 50. The maximum dynamic responses of the structure isolated by NSIABI and traditional base isolator are determined as 2.99 and 8.49. Therefore, the dynamic response reduction capacity of H_2 optimized NSIABI is significantly 64.78 % superior to the traditional base isolator. The variations of the optimal dynamic responses of structures versus frequency ratio isolated by H_∞ optimized NSIABI and traditional base isolator (TBI) subjected to harmonic excitation are shown in Figure 7 (b). For NSIABI, the system parameters are considered as $\mu_b = 0.7$, $\mu_a = 0.1$, $\theta = 14^o$, $\beta = 0.1$, $\eta_b = 0.4451$, and $\zeta_b = 0.2$. For traditional base isolator Jangid (2007); Matsagar and Jangid (2003, 2004), the system parameters are considered as $\mu_b = 0.9$, $\zeta_b = 0.05$, and $T_b = 2.5$ sec, and $\eta_b = 0.4$. The main structural damping ratio considers as $\zeta_s = 0.01$. The maximum dynamic response of the uncontrolled structure obtains as 50. The maximum dynamic responses of the structure isolated by NSIABI and traditional base isolator are determined as 3.65 and 15.97. Therefore, the dynamic response reduction capacity of H_∞ optimized NSIABI is significantly 77.14 % superior to the traditional base isolator. The variations of the optimal dynamic responses of structures versus frequency ratio isolated by H_2 optimized

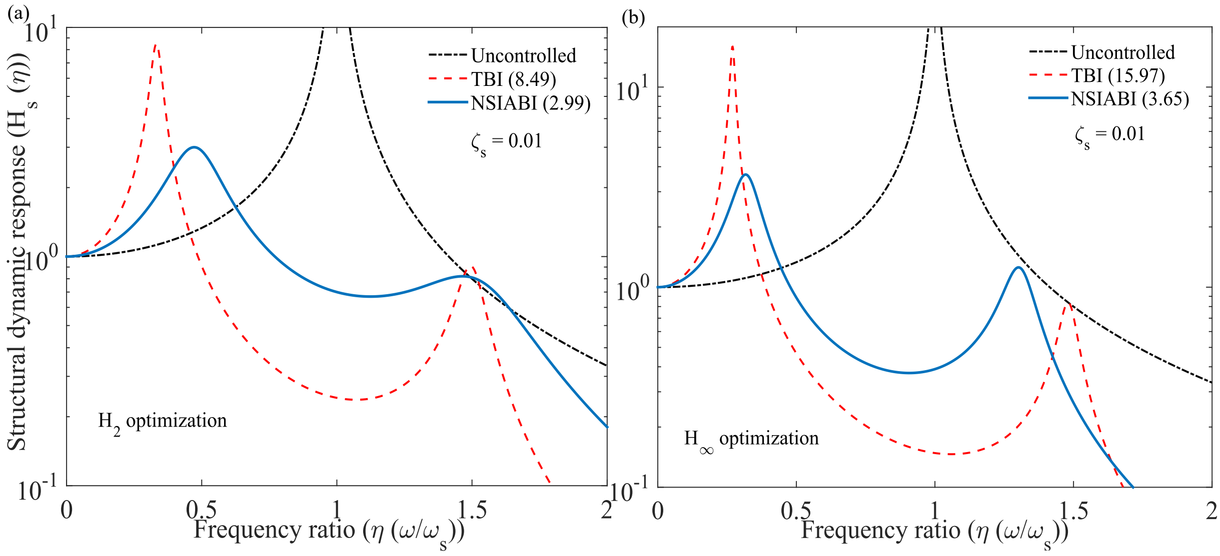

Figure 7: The variations of the optimal dynamic responses of structures versus frequency ratio isolated by H_2 and H_∞ optimized NSIABI and traditional base isolator (TBI) subjected to harmonic excitation.

NSIABI and traditional base isolator (TBI) subjected to random-white noise excitation are shown in Figure 8 (a). According to the dynamic response evaluation, the dynamic response reduction capacity of H_2 optimized NSIABI is significantly 88 % superior to the traditional base isolator. The variations of the optimal dynamic responses of structures

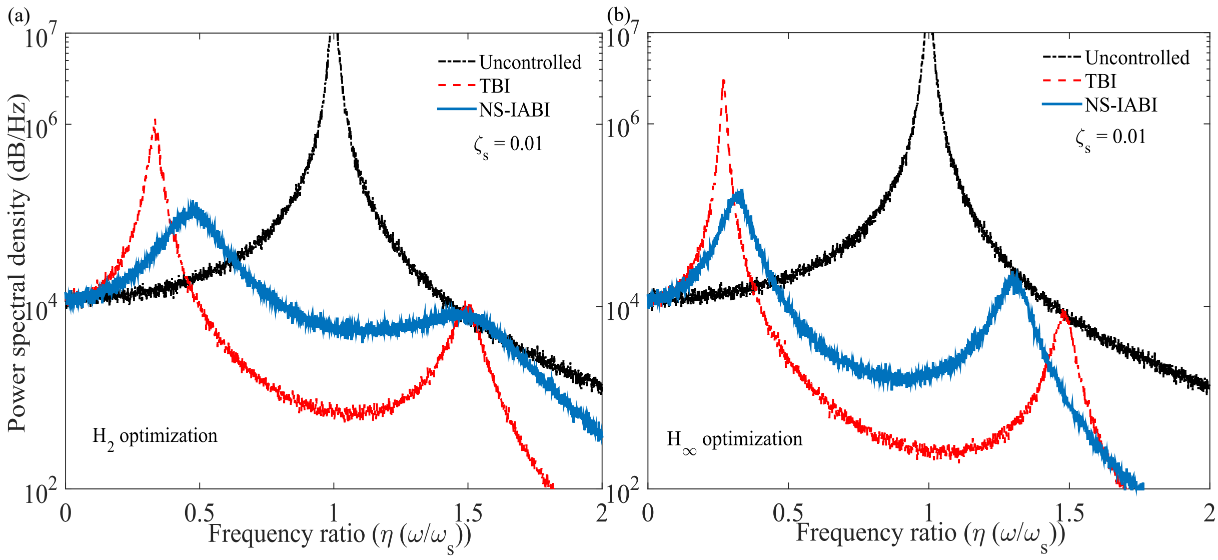

Figure 8: The variations of the optimal dynamic responses of structures vs frequency ratio isolated by H_2 and H_∞ optimized NSIABI and traditional base isolator (TBI) subjected to random white-noise excitation.

versus frequency ratio isolated by H_∞ optimized NSIABI and traditional base isolator (TBI) subjected to random-white noise excitation are shown in Figure 8 (b). According to the dynamic response evaluation, the dynamic response reduction capacity of H_∞

optimized NSIABI is significantly 94.56 % superior to the traditional base isolator.

4. Nonlinear negative stiffness inertial amplifier base isolators for SDOF system

Instead of low amplitude contained vibration, higher amplitude contained vibrations have been applied at the base of the isolated structures. Due to that, the deformation of the amplifier masses derive as

$$x_a = \frac{x_g + u_b}{2} \quad \text{and} \quad y_a = l\sin\theta - \sqrt{l^2\sin^2\theta - x_b l\cos\theta - \frac{x_b^2}{4}} \tag{33}$$

where "l" defines the length of the rigid links, $x_b = u_b - x_g$ defines the relative dynamic response of isolator to base. The velocity response of the amplifier's mass m_a in x and y-directions derive as

$$\dot{x}_a = \frac{\dot{x}_g + \dot{u}_b}{2} \quad \text{and} \quad \dot{y}_a = \frac{(2l\cos\theta + x_b)\dot{x}_b}{\sqrt{16l^2\sin^2\theta - 16x_b l\cos\theta - 4x_b^2}} \tag{34}$$

where ($\bullet$) defines derivative of variables w.r.t time. Using Eq. (34), the total kinetic energy of nonlinear negative stiffness inertial amplifier base isolators (NNSIABI) derives as

$$\begin{aligned} K_e &= \frac{1}{2}m_b\dot{u}_b^2 + 2\times\frac{1}{2}m_a\left(\dot{x}_a^2 + \dot{y}_a^2\right) \\ &= \frac{1}{2}m_b\dot{u}_b^2 + \frac{\gamma m_b\dot{x}_b^2(2l\cos\theta + x_b)^2}{16l^2\sin^2\theta - 16x_b l\cos\theta - 4x_b^2} + \frac{\gamma m_b\left(\dot{x}_g + \dot{u}_b\right)^2}{4} \end{aligned} \tag{35}$$

where $\gamma = m_a/m_b$. The total potential energy derives as

$$P_e = \frac{1}{2}k_b x_b^2 \tag{36}$$

Lagrange's equations Chopra (2007) applies to derive the governing equation of motion for nonlinear NSIABI. Lagrange's equation has been derived as

$$\frac{d}{dt}\left(\frac{\partial K_e}{\partial \dot{x}_j}\right) - \frac{\partial K_e}{\partial x_j} + \frac{\partial P_e}{\partial x_j} + \frac{\partial D}{\partial \dot{x}_j} = 0 \tag{37}$$

where D defines the dissipated energy of the nonlinear NSIABI. x_j defines the generalized version of $x_b = u_b - x_g$ and $x_s = u_s - u_b$, j denotes the subscript for denoting main structure and isolator. x_b and x_s define the relative dynamic response of isolator and structure w.r.t the base and isolator. Therefore, the equations of motion for nonlinear NSIABI derives as

$$\underbrace{\left(1 + \frac{2\gamma l^2}{4l^2\sin^2\theta - 4x_b l\cos\theta - x_b^2}\right)}_{m_{ia}} m_b\,\ddot{x}_b + k_b x_b = -\left(1+\gamma\right)m_b\ddot{x}_g \tag{38}$$

Equation (38) needs to be generalized using the Taylor series for deriving the nonlinear isolated structure's dynamic responses analytically. Therefore, considering the static equilibrium Zhou et al. (2019) (i.e. $x_b = 0$), the effective mass for nonlinear NSIABI derives as

$$m_{ia} = m_{b1} + m_{b2}x_b + m_{b3}x_b^2 = \tau m_b + \frac{\gamma\cos\theta m_b}{2l\sin^4\theta}x_b + \frac{\gamma(1+3\cos^2\theta)m_b}{4l^2\sin^6\theta}x_b^2 \tag{39}$$

where $\tau = 1 + \frac{\gamma}{2\sin^2\theta}$. Hence, after applying Eq. (39) to Eq. (52), the governing equations of motion for the SDOF system isolated by nonlinear NSIABI derive as

$$\begin{aligned} & m_{b1}\ddot{x}_b + 2\zeta_b m_{b1}\omega_b\dot{x}_b + m_{b1}\omega_b^2 x_b - \beta m_{b1}\omega_b^2 x_b + m_{b2}x_b\ddot{x}_b + 2\zeta_b m_{b2}\omega_b x_b\dot{x}_b \\ & + m_{b2}\omega_b^2 x_b^2 - \beta m_{b2}\omega_b^2 x_b^2 + m_{b3}x_b^2\ddot{x}_b + 2\zeta_b m_{b3}\omega_b x_b^2\dot{x}_b + m_{b3}\omega_b^2 x_b^3 - \beta m_{b3}\omega_b^2 x_b^3 \\ & - k_s x_s - c_s\dot{x}_s = -m_{ia}\ddot{x}_g \quad \text{and} \quad m_s\ddot{x}_s + m_s\ddot{x}_b + c_s\dot{x}_s + k_s x_s = -m_s\ddot{x}_g \end{aligned} \tag{40}$$

Equation (64) is a highly nonlinear equation. Therefore, the stochastic linearization method Roberts and Spanos (2003) applies to derive the linearized equations of motion for isolated structures. Therefore, after the application of the stochastic linearization method, the linearized system parameters from Eq. (64) derive as

$$\begin{aligned} k_{b3}^e &= E\left\{\frac{\partial(m_{b3}\omega_b^2 x_b^3)}{\partial x_b}\right\} = 3m_{b3}\omega_b^2\sigma_{x_b}^2 \\ \text{and} \quad k_n^e &= \beta E\left\{\frac{\partial(m_{b3}\omega_b^2 x_b^3)}{\partial x_b}\right\} = 3\beta m_{b3}\omega_b^2\sigma_{x_b}^2 \end{aligned} \tag{41}$$

where $\sigma_{x_b}^2$ defines the standard deviation of the dynamic response of the isolator. Equation (41) is applied to Eq. (64), and the governing equations of motion for the SDOF system isolated by linearized NSIABI derives as

$$\begin{aligned} & m_{b1}\ddot{x}_b + 2\zeta_b m_{b1}\omega_b\dot{x}_b + m_{b1}\omega_b^2 x_b - \beta m_{b1}\omega_b^2 x_b + 3m_{b3}\omega_b^2\sigma_{x_b}^2 x_b \\ & - 3\beta m_{b3}\omega_b^2\sigma_{x_b}^2 x_b - k_s x_s - c_s\dot{x}_s = -m_{b1}\ddot{x}_g \\ & m_s\ddot{x}_s + m_s\ddot{x}_b + c_s\dot{x}_s + k_s x_s = -m_s\ddot{x}_g \end{aligned} \tag{42}$$

The steady-state solutions for the dynamic responses of the isolated structures consider as $x_s = X_s e^{\mathrm{i}\omega t}$, $x_b = X_b e^{\mathrm{i}\omega t}$, and $x_g = X_g e^{\mathrm{i}\omega t}$. Therefore, substituting these solutions into Eq. (42), the transfer function derives as

$$\begin{aligned} & \begin{bmatrix} -\eta^2 + 2\,\mathrm{i}\zeta_s\eta + 1 & -\eta^2 \\ -2\,\mathrm{i}\zeta_s\eta - 1 & C_{22} \end{bmatrix} \begin{Bmatrix} X_s \\ X_b \end{Bmatrix} = -\begin{bmatrix} 1 \\ \mu_{b1} \end{bmatrix} \frac{X_g}{\omega_s^2} \\ & C_{22} = -\mu_{b1}\eta^2 + 2\,\mathrm{i}\zeta_b\mu_{b1}\eta_b\,\eta + {\eta_b}^2\mu_{b1} - \beta{\eta_b}^2\mu_{b1} + \rho \quad \text{and} \quad \rho = 3\mu_{b3}\eta_b^2\tilde{\sigma}_{x_b}^2\,(1-\beta) \end{aligned} \tag{43}$$

where $\tilde{\sigma}_{x_b}^2$ defines the non-dimensional standard deviation of the dynamic response of the main structure. The dynamic response of the main structure obtains as

$$H_s = \frac{X_s}{X_g}\omega_s^2 = \frac{2\,\mathrm{i}\zeta_b\eta\,\eta_b\mu_{b1} - \beta\,{\eta_b}^2\mu_{b1} + {\eta_b}^2\mu_{b1} + \rho}{\Delta} \tag{44}$$

The dynamic response of the linearized NSIABI is obtained as

$$H_b = \frac{X_b}{X_g}\omega_s^2 = \frac{-\mu_{b1}\eta^2 + \mu_{b1} + 1 + \mathrm{i}\,(2\,\zeta_s\eta\,\mu_{b1} + 2\,\zeta_s\eta)}{\Delta} \tag{45}$$

Δ obtains as

$$\Delta = \begin{array}{c} -\beta\,\eta^2{\eta_b}^2\mu_{b1} + 4\,\eta^2\zeta_b\zeta_s\eta_b\mu_{b1} - \eta^4\mu_{b1} + \eta^2{\eta_b}^2\mu_{b1} \\ +\beta\,{\eta_b}^2\mu_{b1} + \eta^2\rho + \mu_{b1}\eta^2 - {\eta_b}^2\mu_{b1} + \eta^2 - \rho \\ +\mathrm{i}\left(\begin{array}{c} 2\,\beta\,\eta\,\zeta_s{\eta_b}^2\mu_{b1} + 2\,\eta^3\zeta_b\eta_b\mu_{b1} + 2\,\eta^3\zeta_s\mu_{b1} \\ -2\,\eta\,\zeta_s{\eta_b}^2\mu_{b1} + 2\,\eta^3\zeta_s - 2\,\zeta_b\eta\,\eta_b\mu_{b1} - 2\,\eta\,\rho\,\zeta_s \end{array}\right) \end{array} \tag{46}$$

Using Eq. (45), Eq. (46), Eq. (12), and Eq. (13), $\sigma^2_{x_b}$ for SDOF system derives Chowdhury et al. (2022) and expressed as

$$\sigma^2_{x_b} = \frac{S_0\pi\,\left(\beta\,\mu_{b1}{\omega_b}^2 - {\mu_{b1}}^2{\omega_s}^2 - {\omega_b}^2\mu_{b1} - 2\,\mu_{b1}{\omega_s}^2 - {\omega_s}^2\right)}{2\zeta_b{\mu_{b1}}^2{\omega_b}^3{\omega_s}^2\,(\beta - 1)} \tag{47}$$

The non-dimensional form of Eq. (47) obtains as

$$\tilde{\sigma}^2_{x_b} = \left(\frac{S_0\pi}{\omega_s^3}\right)\frac{\left({\mu_{b1}}^2 + {\eta_b}^2\mu_{b1} + 2\,\mu_{b1} + 1 - \beta\,\mu_{b1}{\eta_b}^2\right)}{2\zeta_b{\mu_{b1}}^2{\eta_b}^3\,(1 - \beta)} \tag{48}$$

Substituting Eq. (48) and Eq. (39) to Eq. (43), ρ determines as

$$\rho = \left(\frac{3\eta_b^2(1 + 3\cos^2\theta)m_a}{4l^2\sin^6\theta}\right)\left(\frac{S_0\pi}{\omega_s^3}\right)\left(\frac{{\mu_{b1}}^2 + {\eta_b}^2\mu_{b1} + 2\,\mu_{b1} + 1 - \beta\,\mu_{b1}{\eta_b}^2}{2\zeta_b{\mu_{b1}}^2{\eta_b}^3}\right) \tag{49}$$

The variations of optimal dynamic responses of structures vs frequency ratio isolated by H_2 optimized nonlinear NSIABI shows in Figure 9 (a). The variations of optimal dynamic

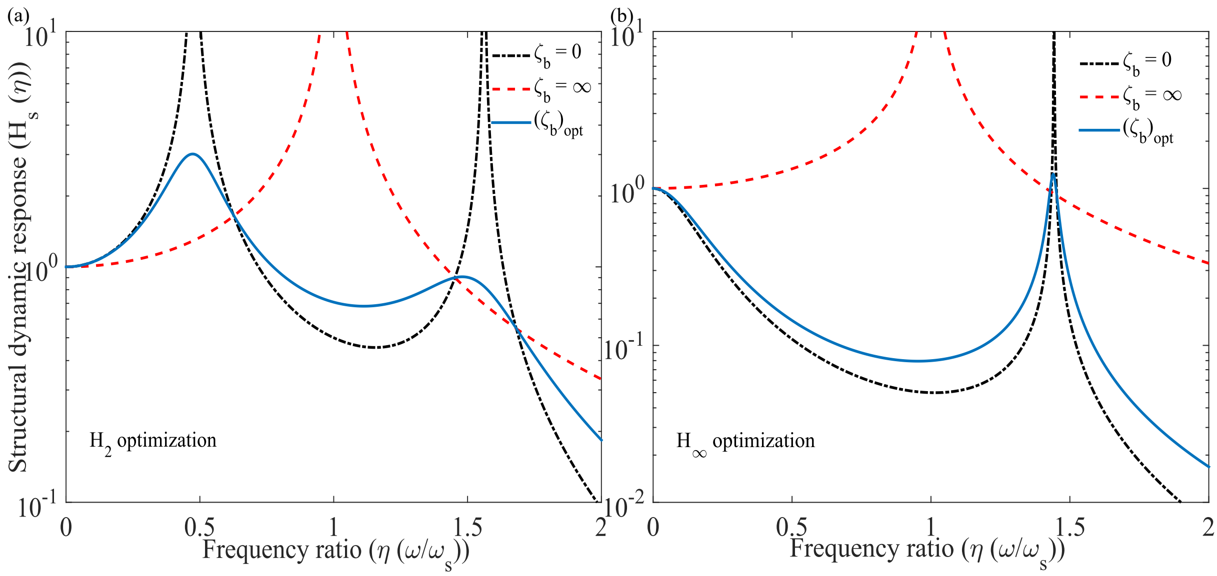

Figure 9: The variations of optimal dynamic responses of structures vs frequency ratio isolated by (a) H_2 and (b) H_∞ optimized nonlinear NSIABI.

responses of structures vs frequency ratio isolated by H_∞ optimized nonlinear NSIABI shows in Figure 9 (b). The variations of optimal dynamic responses of structures vs frequency ratio isolated by H_2 optimized nonlinear NSIABI and traditional base isolator subjected to harmonic base excitation show in Figure 10 (a). The maximum dynamic responses of the main structures have been determined as 8.49 and 3.00. Therefore, H_2 optimized nonlinear NSIABI is significantly 64.66 % superior to the H_2 optimized traditional base isolator. The variations of optimal dynamic responses of structures vs frequency ratio isolated by H_∞ optimized nonlinear NSIABI and traditional base isolator subjected to harmonic base excitation show in Figure 10 (b). The maximum dynamic responses of the main structures have been determined as 15.97 and 5.34. Therefore,

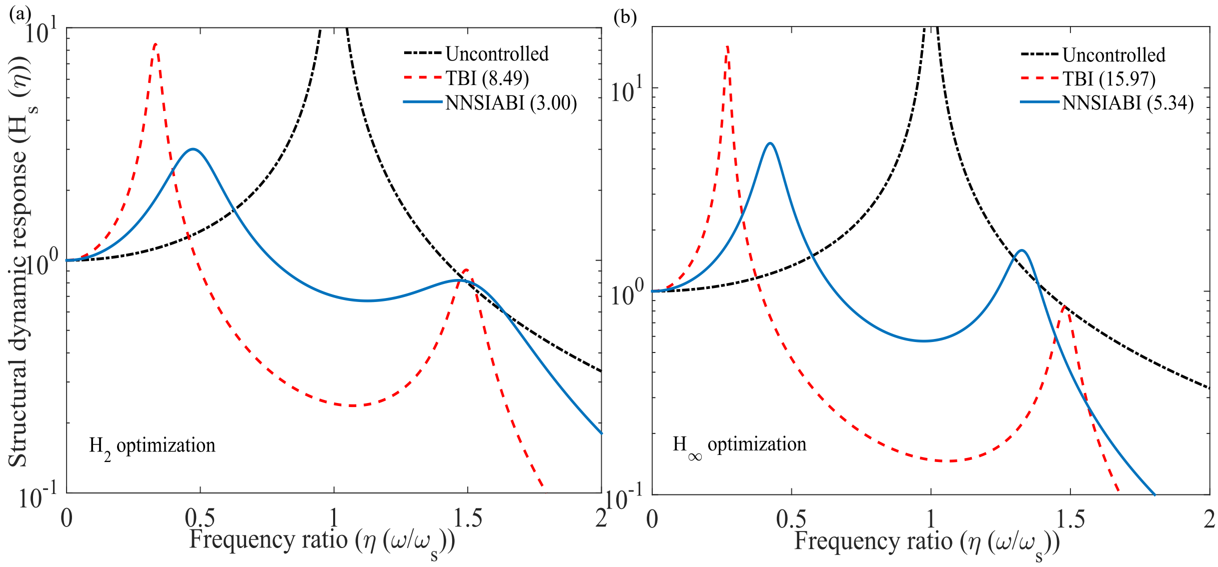

Figure 10: The variations of optimal dynamic responses of structures vs frequency ratio isolated by (a) H_2 and (b) H_∞ optimized nonlinear NSIABI and traditional base isolator subjected to harmonic base excitation.

H_∞ optimized nonlinear NSIABI is significantly 66.56 % superior to the H_∞ optimized traditional base isolator. The dynamic response reduction capacity of NNSIABI has also been determined for random-white noise excitation. Hence, the variations of optimal dynamic responses of structures vs frequency ratio isolated by H_2 optimized nonlinear NSIABI and traditional base isolator subjected to random base excitation show in Figure 11 (a). The variations of optimal dynamic responses of structures vs frequency ratio

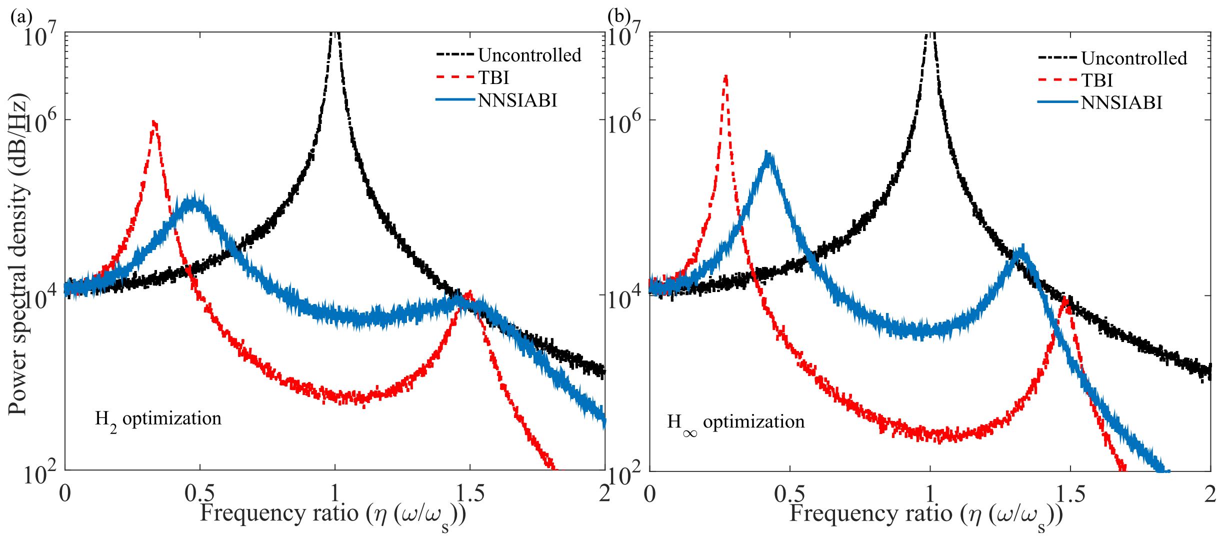

Figure 11: The variations of optimal dynamic responses of structures vs frequency ratio isolated by (a) H_2 optimized and (b) H_∞ optimized nonlinear NSIABI and traditional base isolator subjected to random base excitation.

isolated by H_∞ optimized nonlinear NNSIABI and traditional base isolator subjected to random base excitation show in Figure 11 (b). The maximum dynamic response of H_2 and H_∞ optimized-controlled structure's dynamic responses are lesser than the optimum traditional base isolators. Therefore, the dynamic response reduction capacity of optimum NNSIABI is significantly higher than the optimum traditional base isolated subjected to random-white noise excitation.

5. Time history results

Through a numerical investigation, the correctness of the H_2 and H_∞ optimised closed-form formulas for the best design parameters for NNSIABI has been confirmed. The numerical analysis was conducted using the Newmark-beta approach. In order to ascertain the dynamic reactions of the uncontrolled and isolated structures, eleven near-field genuine earthquake base excitations (Pulse recordings) were obtained from the Pacific Earthquake Engineering Research Centre (https://peer.berkeley.edu/peer-strong-ground-motion-databases) and induced in the MATLAB programmes. Table 1 contains a full list of the near field earthquake recordings' attributes. These data were used to create and present in Figure 12

Table 1: Details of near-field earthquake base excitations (Pulse records) (https://peer.berkeley.edu/peer-strong-ground-motion-databases).

Earthquake	Year	M_w	Recording station	Vs_{30}(m/s)	Component	E_s (km)	PGA,g
Irpinia, Italy-01	1980	6.9	Sturno	1000	MUL009	30.4	0.31
Superstition Hills-02	1987	6.5	Parachute Test Site	349	SUPERST	16.0	0.42
Loma Prieta	1989	6.9	LOMAP	371	HEC000	27.2	0.38
Erzican, Turkey	1992	6.7	Erzincan 11	275	ERZIKAN	9.0	0.49
Cape Mendocino	1992	7.0	CAPEMEND	713	NIS090	4.5	0.63
Landers	1992	7.3	Lucerne	685	LANDERS	44.0	0.79
Northridge-01	1994	6.7	Rinaldi Receiving Sta	282	NORTHR	10.9	0.87
Kocaeli, Turkey	1999	7.5	Izmit	811	KOCAELI	5.3	0.22
Chi-Chi, Taiwan	1999	7.6	TCU065	306	CHICHI	26.7	0.82
Chi-Chi, Taiwan	1999	7.6	TCU102	714	CHICHI	45.6	0.29
Duzce, Turkey	1999	7.1	Duzce	276	DUZCE	1.6	0.52

the response spectra Banerjee et al. (2017) at 5% damping for all near-field earthquake base excitations (Pulse recordings). Every earthquake spectrum has a larger amplitude and experiences brief frequency fluctuations. For the structures, this is more damaging than the far-filed earthquake. If the new isolators can be used to reduce the vibration caused by near-field earthquakes, then the buildings will also be protected from far-field earthquakes. Therefore, in order to acquire the dynamic reactions of the buildings, near-field with pulses earthquake data are utilised in the MATLAB environment. This numerical analysis has been conducted using the Newmark-beta approach. The changes in the displacement and acceleration responses versus time of the uncontrolled and isolated structures are shown in Figure 13 (a) and Figure 13 (b). The maximum displacement responses are determined for all structures and listed in Table 2. The maximum displacement of main buildings with corresponding displacement reduction of each H_2 optimized isolator w.r.t uncontrolled building ($D_r(\%)$) under near-field earthquake base excitations

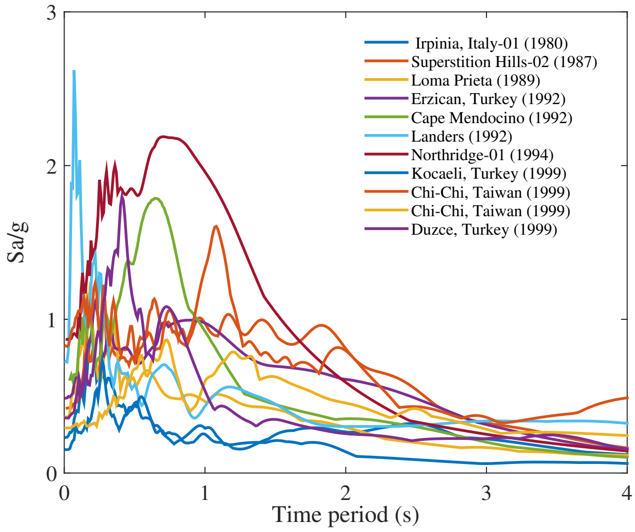

Figure 12: Response spectra of eleven near-field earthquake records (5% damped).

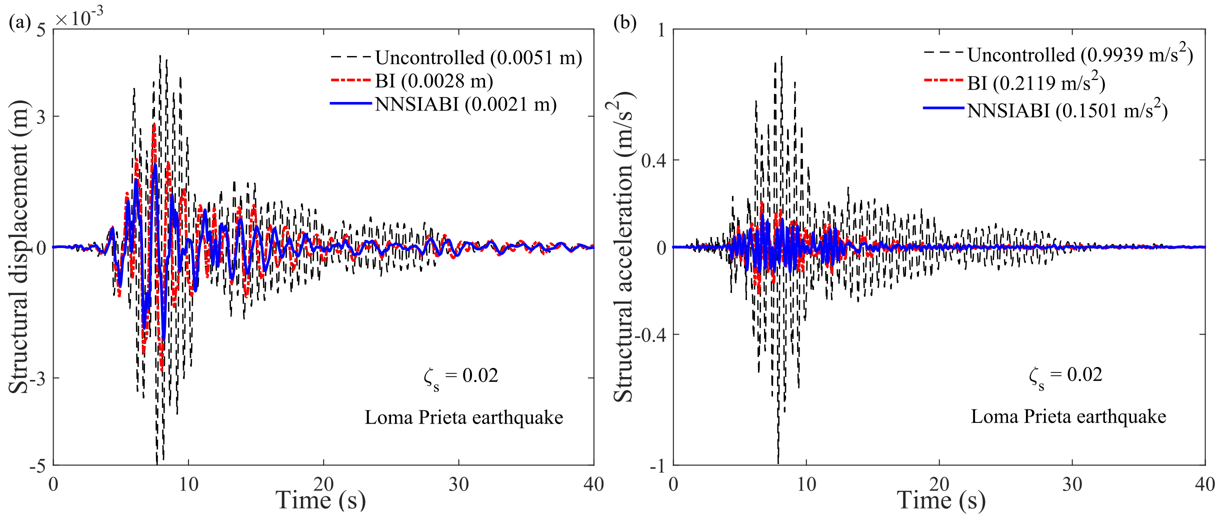

Figure 13: The (a) displacement and (b) acceleration responses of structures vs time isolated by optimum NNSIABI subjected to Loma Prieta earthquake.

has been listed in Table 2.

$$D_r(\%) = \frac{(x_s^{max})_{TBI} - (x_s^{max})_{NNSIABI}}{(x_s^{max})_{TBI}} \tag{50}$$

where $(x_s^{max})_{TBI}$ refers to the maximum displacement of the SDOF system isolated by TBI. $(x_s^{max})_{NNSIABI}$ refers to the maximum displacement of the SDOF system isolated by NNSIABI. According to this result, the proposed NNSIABI has 23.42 % more vibration reduction capacity than the traditional base isolator (TBI). Similarly, the maximum acceleration responses of the uncontrolled and isolated structures are determined and listed in Table 3. The maximum acceleration of main buildings with corresponding acceleration reduction of each optimum isolator w.r.t uncontrolled building ($A_r(\%)$) under near-field

Table 2: Under near-field earthquake base excitations (Pulse recordings), the maximum displacement responses of the main building x_s^{max} (m) and the associated displacement reduction of each optimal isolator with respect to the uncontrolled building ($D_r(\%)$) .

Earthquake	x_s^{max} **(m)**			$D_r(\%)$
	Uncontrolled	**TBI Matsagar and Jangid (2003)**	**NNSIABI**	**NNSIABI**
Irpinia, Italy-01	0.0041	0.0013	0.0011	15.23
Superstition Hills-02	0.0067	0.0052	0.0042	19.11
Loma Prieta	0.0051	0.0028	0.0021	25.08
Erzican, Turkey	0.0063	0.0023	0.0019	17.70
Cape Mendocino	0.0094	0.0059	0.0037	37.31
Landers	0.0045	0.0032	0.0028	14.23
Northridge-01	0.0122	0.0113	0.0076	32.46
Kocaeli, Turkey	0.0041	0.0014	0.0011	22.71
Chi-Chi, Taiwan	0.0088	0.0062	0.0036	40.87
Chi-Chi, Taiwan	0.0052	0.0040	0.0033	17.54
Duzce, Turkey	0.0081	0.0032	0.0027	15.37
Average	0.0067	0.0042	0.0031	23.42

earthquake base excitations has been listed in Table 3.

Table 3: Under near-field earthquake base excitations (Pulse recordings), the maximum acceleration responses of the main building $\ddot{x}_s^{max}$ (m/s^2) and the corresponding acceleration reduction of each optimal isolator with respect to the uncontrolled building ($A_r(\%)$).

Earthquake	$\ddot{x}_s^{max}$ (m/s^2)			$A_r(\%)$
	Uncontrolled	**TBI Matsagar and Jangid (2003)**	**NNSIABI**	**NNSIABI**
Irpinia, Italy-01	0.5981	0.1556	0.0952	38.86
Superstition Hills-02	0.9902	0.2206	0.1950	11.61
Loma Prieta	0.9939	0.2119	0.1501	29.17
Erzican, Turkey	0.9005	0.2733	0.169	38.15
Cape Mendocino	1.4537	0.4055	0.3207	20.92
Landers	1.0335	0.2315	0.1536	33.63
Northridge-01	2.1397	0.5917	0.4004	32.33
Kocaeli, Turkey	0.6587	0.1249	0.0762	39.03
Chi-Chi, Taiwan	1.0941	0.3269	0.208	36.37
Chi-Chi, Taiwan	0.6910	0.1551	0.1469	5.24
Duzce, Turkey	0.9397	0.3932	0.2400	38.96
Average	1.045	0.2809	0.1959	29.48

$$A_r(\%) = \frac{(\ddot{x}_s^{max})_{TBI} - (\ddot{x}_s^{max})_{NNSIABI}}{(\ddot{x}_s^{max})_{TBI}} \tag{51}$$

where $(\ddot{x}_s^{max})_{TBI}$ refers to the maximum acceleration of the SDOF system isolated by TBI. $(\ddot{x}_s^{max})_{NNSIABI}$ refers to the maximum acceleration of the SDOF system isolated by NNSIABI. According to that, the proposed NNSIABI has 29.48 % more vibration reduction capacity than TBI. The histogram of the uncontrolled and isolated structures using their displacement and acceleration responses are shown in Figure 14 (a) and Figure 14 (b). The maximum dynamic responses of the isolated structures are divided by

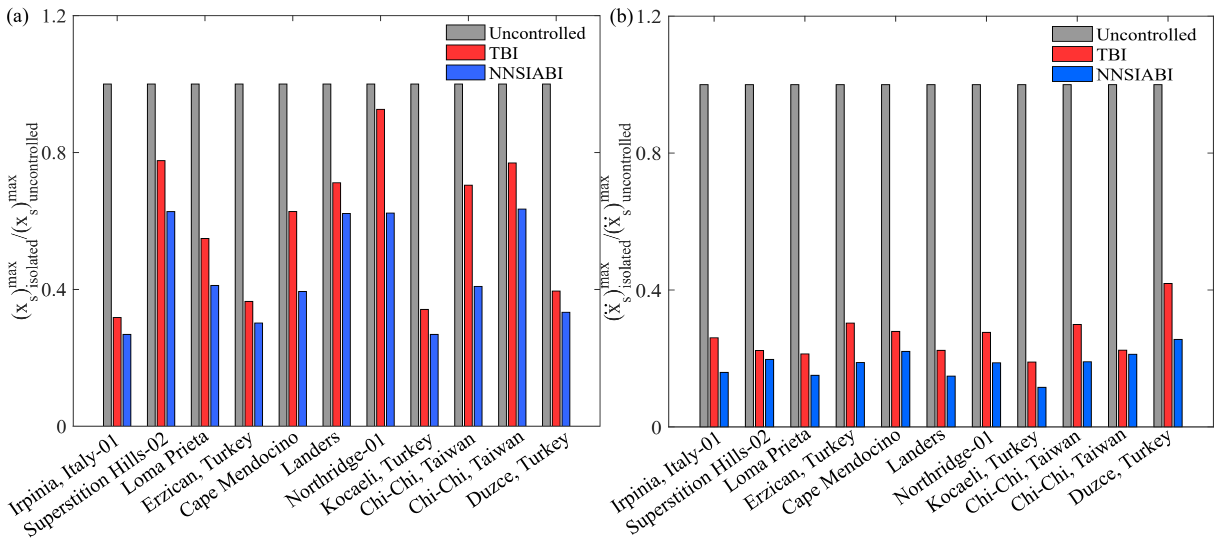

Figure 14: The bar diagrams of (a) displacement and (b) acceleration of structure isolated by TBI and NNSIABI.

the maximum dynamic responses of the uncontrolled structures. The ratios are applied to obtain the histogram diagrams. The histogram plots of the NNSIABI-isolated structures are much smaller than the histogram diagrams of the uncontrolled structures and structures isolated by TBI. The variations of the structural damping force versus structural displacement are shown in Figure 15 (a). The value for structural damping is considered as 0.02, i.e. $\zeta_s = 0.02$. Each isolated structure's damping force versus structural displacement curve is smaller than the uncontrolled structure. Precisely, the NNSIABI-isolated structure's damping curve is smaller than the TBI-isolated structure's damping curve. Hence, the damping force reduction capacity of NNSIABI is more than the damping force reduction capacity of TBI. In addition, the energy dissipation capacity of each isolator is obtained separately to visualise the energy flow within the structures during an earthquake. Therefore, the variations of the normalised energy of structure versus time are shown in Figure 15 (b). The kinetic energy, dissipated energy, and potential energy of the uncontrolled structure is obtained analytically. The potential energy is slightly more than the dissipated and kinetic energies. The maximum amplitudes of each energy plot are near 0.57 to 0.59 ranges. In addition, the energy plots of each isolated structure are derived. Therefore, the variations of the normalised energy of the structures isolated by TBI and NNSIABI versus time are shown in Figure 16 (a) and Figure 16 (b). In Figure 16 (a), the potential energy plot has a maximum amplitude of 0.2, whereas in Figure 16 (b), the potential energy plot has a maximum amplitude of 0.1. The kinetic and dissipated energy plots are also following the same trends. The rest of the energy is dissipated outside the environment through mechanical energy to thermal energy during earthquake and post-earthquake scenarios. Therefore, the proposed NNSIABI is more effective than TBI in terms of vibration reduction capacity.

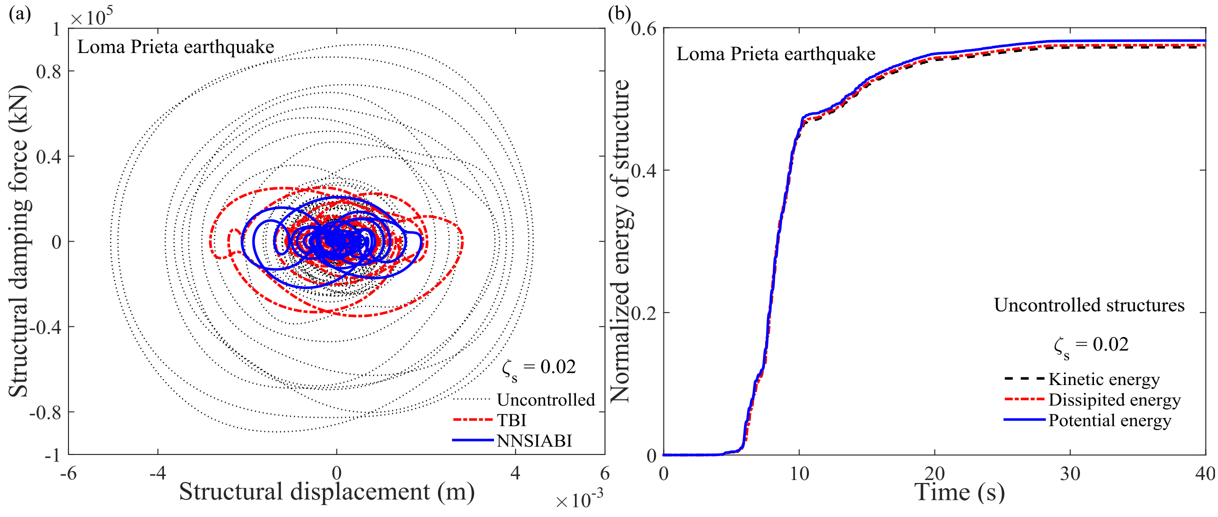

Figure 15: (a) The variations of structural damping force versus structural displacement. (b) The normalized energy of structure versus time.

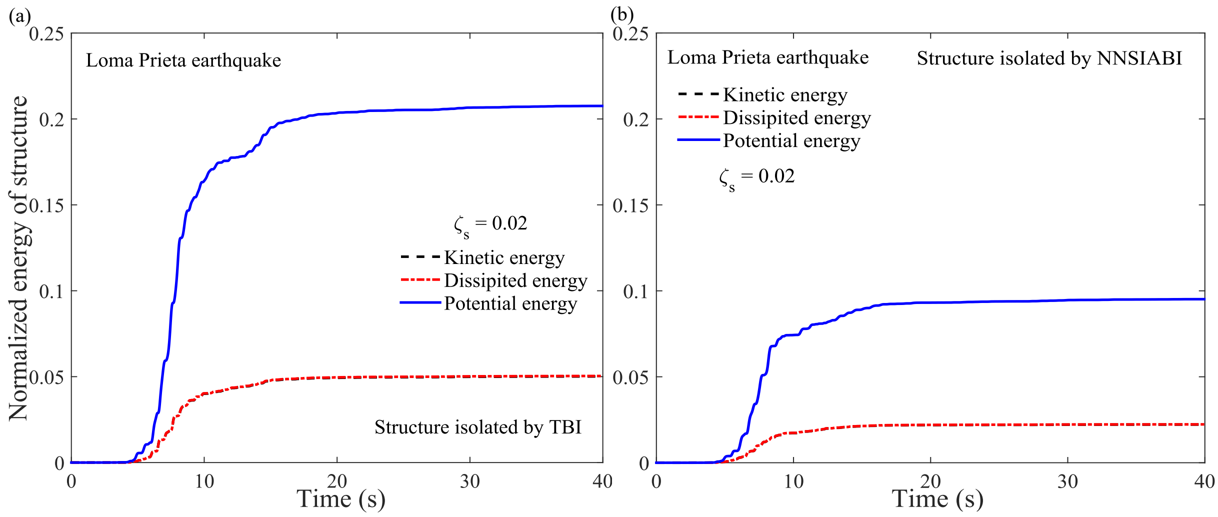

Figure 16: The changes in the normalised energy of structure isolated by (a) TBI and (b) NNSIABI versus time.

6. Negative stiffness inertial amplifier base isolators for multi-storey building

The negative stiffness inertial amplifier base isolators (NSIABI) are applied to multi-storey buildings to mitigate their dynamic responses. Therefore, the structural diagram of a multi-storey building isolated by negative stiffness inertial amplifier base isolator subjected to base excitation has been shown in Figure 17. Newton's second law has been applied to derive the governing equations of motion for the multi-storey buildings isolated by NSIABI. Therefore, the equations of motion of NSIABI for multi-storey buildings subjected to base excitation are derived as

$$\begin{aligned}
&[\mathbf{M}_s]\{\ddot{\mathbf{x}}_s\} + [\mathbf{C}_s]\{\dot{\mathbf{x}}_s\} + [\mathbf{K}_s]\{\mathbf{x}_s\} = -[\mathbf{M}_s]\{\mathbf{r}\}(\ddot{x}_g + \ddot{x}_b) \\
&m_{ia}\ddot{x}_b + c_{ia}\dot{x}_b + k_{ia}x_b - k_n x_b - k_1 x_1 - c_1\dot{x}_1 = -m_{ia}\ddot{x}_g
\end{aligned} \tag{52}$$

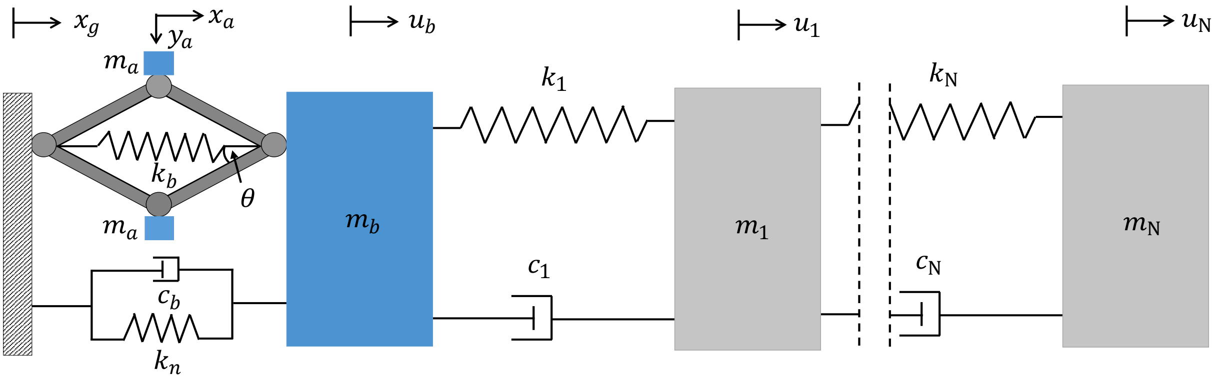

Figure 17: The structural diagram of a multi-storey building isolated by negative stiffness inertial amplifier base isolator subjected to base excitation.

where $x_b = u_b - x_g$ defines the relative dynamic response of isolator to base. $x_N = u_N - u_b$, $x_{N-1} = u_{N-1} - u_b$, and $x_1 = u_1 - u_b$ define the relative dynamic response of each floor w.r.t the isolator. $[\mathbf{M}_s]$, $[\mathbf{C}_s]$, and $[\mathbf{K}_s]$ define the mass, damping, and stiffness matrices of the superstructure. $\{\mathbf{x}_s\} = \{x_1, x_2, x_3, \cdots, x_N\}$, $\{\ddot{\mathbf{x}}_s\}$, and $\{\dot{\mathbf{x}}_s\}$ are the main structure's unknown vectors for each degree of freedom, such as displacement, acceleration, and velocity vectors. $(\dot{\bullet})$ define the derivative of variables w.r.t time. The influence coefficient vector for loading function considers as $\{\mathbf{r}\} = \{1, 1, 1, \cdots, 1\}$. Initially, the mathematical model of a five-storey building is considered to derive the closed-form expressions for optimal design parameters of IABI analytically. To derive the exact closed-form expressions for optimal design parameters of NSIABI analytically in a simplified manner, the mass, stiffness, and damping of each floor are considered as m_s (i.e., $m_1 = m_2 = m_3 = m_4 = m_5 = m_s$), k_s (i.e., $k_1 = k_2 = k_3 = k_4 = k_5 = k_s$), and c_s (i.e., $c_1 = c_2 = c_3 = c_4 = c_5 = c_s$). The steady-state solutions are considered as $x_1 = X_1 e^{\mathrm{i}\omega t}$, $x_2 = X_2 e^{\mathrm{i}\omega t}$, $x_3 = X_3 e^{\mathrm{i}\omega t}$, $x_4 = X_4 e^{\mathrm{i}\omega t}$, $x_5 = X_5 e^{\mathrm{i}\omega t}$, $x_b = X_b e^{\mathrm{i}\omega t}$, and $\ddot{x}_g = X_g e^{\mathrm{i}\omega t}$. Using the steady-state solutions, the transfer function derives as

$$\begin{bmatrix} A_1 & A_2 & 0 & 0 & 0 & q^2 \\ A_2 & A_1 & A_2 & 0 & 0 & q^2 \\ 0 & A_2 & A_1 & A_2 & 0 & q^2 \\ 0 & 0 & A_2 & A_1 & A_2 & q^2 \\ 0 & 0 & 0 & A_2 & A_3 & q^2 \\ A_2 & 0 & 0 & 0 & 0 & A_4 \end{bmatrix} \begin{Bmatrix} X_1 \\ X_2 \\ X_3 \\ X_4 \\ X_5 \\ X_b \end{Bmatrix} = - \begin{bmatrix} 1 \\ 1 \\ 1 \\ 1 \\ 1 \\ \mu_{ia} \end{bmatrix} X_g \tag{53}$$

$$\begin{aligned} & q = \mathrm{i}\omega, A_1 = 4\,\zeta_s q \omega_s + q^2 + 2\,{\omega_s}^2, A_2 = -2\,\zeta_s q \omega_s - {\omega_s}^2, \\ & A_3 = 2\,\zeta_s q \omega_s + q^2 + {\omega_s}^2 \quad \text{and} \quad A_4 = 2\,\zeta_b q \omega_b \mu_{ia} + q^2 \mu_{ia} + \mu_{ia} {\omega_b}^2 - \beta\, {\omega_b}^2 \mu_{ia} \end{aligned} \tag{54}$$

where $\mu_b = m_b/m_s$ defines the base mass ratio and $\mu_{ia} = m_{ia}/m_s$ defines the effective base mass ratio. $\mu_a = m_a/m_s$ defines the amplifiers mass ratio. $\eta_b = \omega_b/\omega_s$ defines the isolator frequency ratio. Each floor's frequency and damping ratio obtain as $\omega_s = \sqrt{k_s/m_s}$ and $\zeta_s = \frac{c_s}{2 m_s \omega_s}$. Each floor's damping ratio considers as 0, i.e., $\zeta_s = 0$ to reduce the length of the closed-form expressions for isolated structure's dynamic responses.

These mathematical simplifications also help to derive the optimal closed-form solutions for design parameters in a simplified manner, and only the isolator's optimal system parameters have been achieved in the closed-form expressions. Therefore, the dynamic response of the top floor derives as

$$H_5(q) = \frac{X_5}{X_g} = \frac{\left(\begin{array}{c} \mu_{ia}\left(q^2+{\omega_s}^2\right)\omega_b\left(q^2+3\,{\omega_s}^2\right) \\ \left(q^4+5\,q^2{\omega_s}^2+5\,{\omega_s}^4\right)\left(\omega_b\beta-2\,q\zeta_b-\omega_b\right) \end{array}\right)}{\Delta} \tag{55}$$

The dynamic response of NSIABI derives as

$$H_b(q) = \frac{X_b}{X_g} = \frac{\left(\begin{array}{c} q^{10}\mu_{ia}+9\,{\omega_s}^2q^8\mu_{ia}+28\,{\omega_s}^4q^6\mu_{ia}+35\,{\omega_s}^6q^4\mu_{ia} \\ +15\,{\omega_s}^8q^2\mu_{ia}+\mu_{ia}{\omega_s}^{10}+{\omega_s}^2q^8+8\,{\omega_s}^4q^6 \\ +21\,{\omega_s}^6q^4+20\,{\omega_s}^8q^2+5\,{\omega_s}^{10} \end{array}\right)}{\Delta} \tag{56}$$

The closed-form expression for Δ has been derived as

$$\Delta = \left(\begin{array}{c} q^{12}\mu_{ia}+2\,q^{11}\zeta_b\mu_{ia}\omega_b+18\,q^9\zeta_b\mu_{ia}\omega_b{\omega_s}^2 \\ +\left(-\beta\,\mu_{ia}{\omega_b}^2+\mu_{ia}{\omega_b}^2+9\,\mu_{ia}{\omega_s}^2+{\omega_s}^2\right)q^{10} \\ +\left(-9\,\beta\,\mu_{ia}{\omega_b}^2{\omega_s}^2+9\,\mu_{ia}{\omega_b}^2{\omega_s}^2+28\,\mu_{ia}{\omega_s}^4+8\,{\omega_s}^4\right)q^8 \\ +56\,q^7\zeta_b\mu_{ia}\omega_b{\omega_s}^4 \\ +\left(-28\,\beta\,\mu_{ia}{\omega_b}^2{\omega_s}^4+28\,\mu_{ia}{\omega_b}^2{\omega_s}^4+35\,\mu_{ia}{\omega_s}^6+21\,{\omega_s}^6\right)q^6 \\ +70\,q^5\zeta_b\mu_{ia}\omega_b{\omega_s}^6 \\ +\left(-35\,\beta\,\mu_{ia}{\omega_b}^2{\omega_s}^6+35\,\mu_{ia}{\omega_b}^2{\omega_s}^6+15\,\mu_{ia}{\omega_s}^8+20\,{\omega_s}^8\right)q^4 \\ +30\,q^3\zeta_b\mu_{ia}\omega_b{\omega_s}^8 \\ +\left(-15\,\beta\,\mu_{ia}{\omega_b}^2{\omega_s}^8+15\,\mu_{ia}{\omega_b}^2{\omega_s}^8+\mu_{ia}{\omega_s}^{10}+5\,{\omega_s}^{10}\right)q^2 \\ +2\,q\zeta_b\mu_{ia}\omega_b{\omega_s}^{10}-\beta\,\mu_{ia}{\omega_b}^2{\omega_s}^{10}+\mu_{ia}{\omega_b}^2{\omega_s}^{10} \end{array}\right) \tag{57}$$

6.1. H_2 optimization for white-noise random excitation

H_2 optimization method applies to derive the optimal closed-form solutions for design parameters of multi-storey buildings isolated by NSIABI Chowdhury et al. (2022). The standard deviation of the dynamic response of the main structure's top floor has been derived using Eq. (55), Eq. (57) and expressed as

$$\sigma_{x_5}^2 = \frac{S_0\omega_b\pi\left(\begin{array}{c} 671\,\beta^2\mu_{ia}{\omega_b}^2+220\,\mu_{ia}{\zeta_b}^2{\omega_s}^2-1342\,\beta\,{\omega_b}^2\mu_{ia} \\ -225\,\beta\,{\omega_s}^2+671\,\mu_{ia}{\omega_b}^2+225\,{\omega_s}^2 \end{array}\right)}{2\zeta_b{\omega_s}^6} \tag{58}$$

The equation below has been used to determine the optimal NSIABI design parameters for structures.

$$\frac{\partial\sigma_{x_5}^2}{\partial\zeta_b} = 0 \quad \text{and} \quad \frac{\partial\sigma_{x_5}^2}{\partial\omega_b} = 0 \tag{59}$$

By substituting $\sigma_{x_s}^2$ into the first equation of Eq. (59), the closed-form expression for damping ratio of NSIABI ζ_b has been derived and expressed as

$$\zeta_b = \frac{\sqrt{55}\sqrt{\mu_{ia}\left(671\,\beta^2\mu_{ia}{\omega_b}^2-1342\,\beta\,{\omega_b}^2\mu_{ia}-225\,\beta\,{\omega_s}^2+671\,\mu_{ia}{\omega_b}^2+225\,{\omega_s}^2\right)}}{110\,\mu_{ia}\omega_s} \tag{60}$$

Equation (60) contains optimal frequency of NSIABI ω_b which needs to to be separated. To achieve that, Eq. (60) has been substituted in Eq. (58). Therefore, the modified standard deviation of displacement response has been derived as

$$\sigma_{x_5}^2 = \frac{2\sqrt{671}\mu_{ia}(\beta-1)\sqrt{55}\omega_b S_0 \pi \left(671\,\beta\,\omega_b{}^2\mu_{ia} - 671\,\mu_{ia}\omega_b{}^2 - 225\,\omega_s{}^2\right)}{671\sqrt{\mu_{ia}(\beta-1)\left(\omega_b{}^2(\beta-1)\mu_{ia} - \frac{225\,\omega_s{}^2}{671}\right)}\omega_s{}^5} \tag{61}$$

Equation (61) substitutes in the second equation of Eq. (59). Therefore, the closed-form expression for the optimal natural frequency of the NSIABI has been derived as

$$(\omega_b)_{\text{opt}} = \frac{15\omega_s}{\sqrt{1342\,\mu_{ia} - 1342\,\beta\,\mu_{ia}}} \tag{62}$$

Equation (62) substitutes in Eq. (60) to derive the exact closed-form expression for the optimal damping ratio of NSIABI and expressed as

$$(\zeta_b)_{\text{opt}} = \frac{3\sqrt{(1-\beta)\,\mu_{ia}}\sqrt{330}}{44\,\mu_{ia}} \tag{63}$$

The variations of optimal frequency ratio of NSIABI for five-storey buildings with different values of amplifier mass ratio show in Figure 18 (a). The variations of optimal frequency

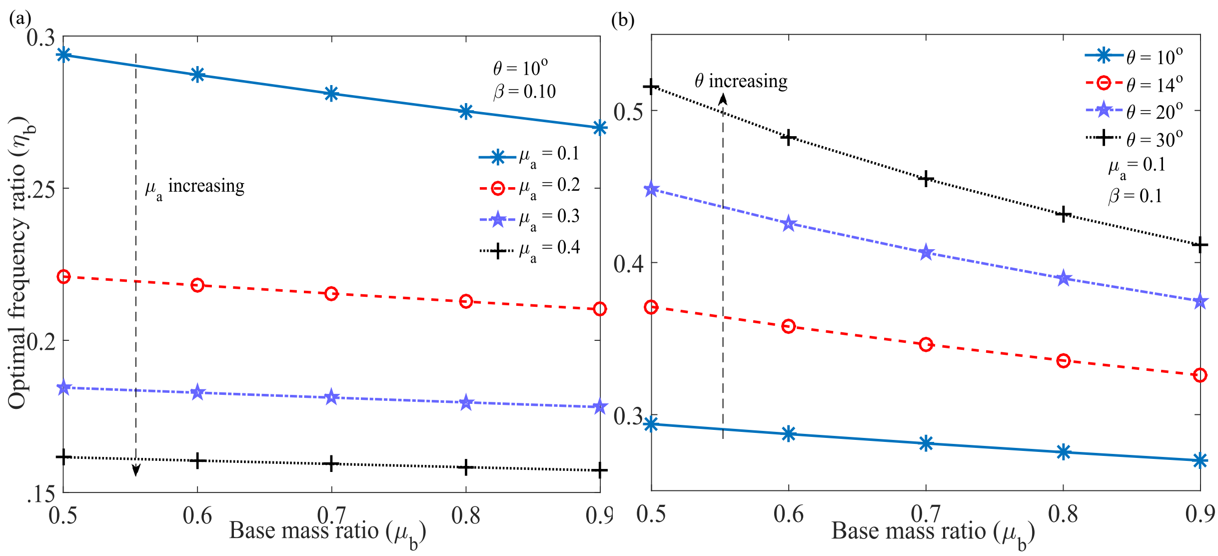

Figure 18: The variations of optimal frequency ratio of NSIABI for five-storey buildings with different values of (a) amplifier mass ratio and (b) inertial angle.

ratio of NSIABI for five-storey buildings with different values of inertial angle show in Figure 18 (b). The variations of optimal damping ratio of NSIABI for five-storey buildings with different values of amplifier mass ratio show in Figure 19 (a). The variations of optimal damping ratio of NSIABI for five-storey buildings with different values of inertial angle show in Figure 19 (b). The variations of optimal dynamic responses of the top floor of the five storey vs frequency ratio isolated by optimum NSIABI for different values of damping ratio show in Figure 20 (a). The variations of optimal dynamic responses of the

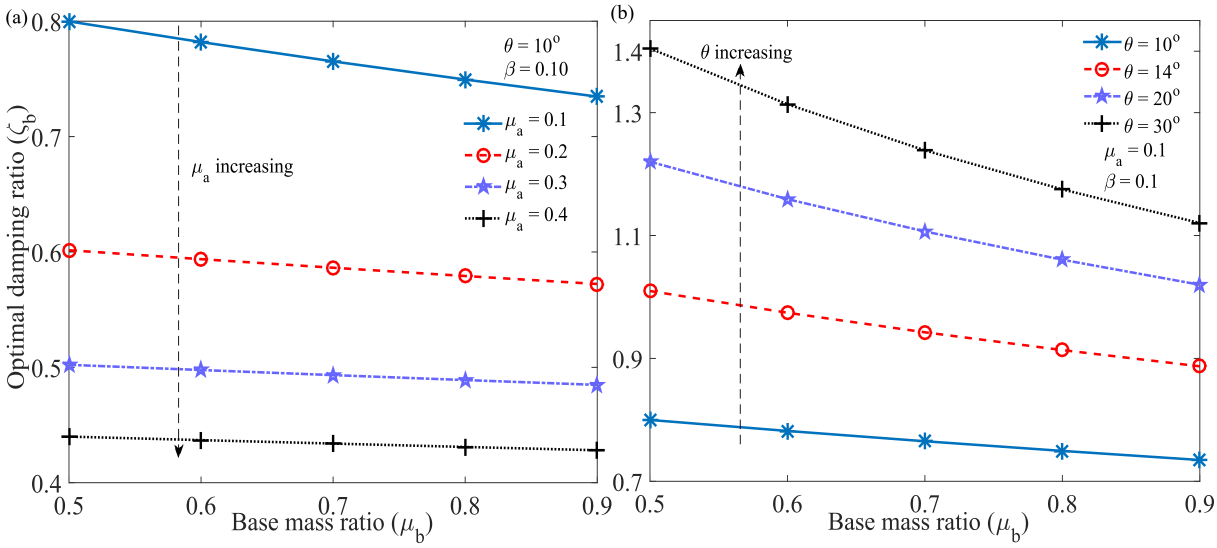

Figure 19: The variations of optimal damping ratio of NSIABI for five-storey buildings with different values of (a) amplifier mass ratio and (b) inertial angle.

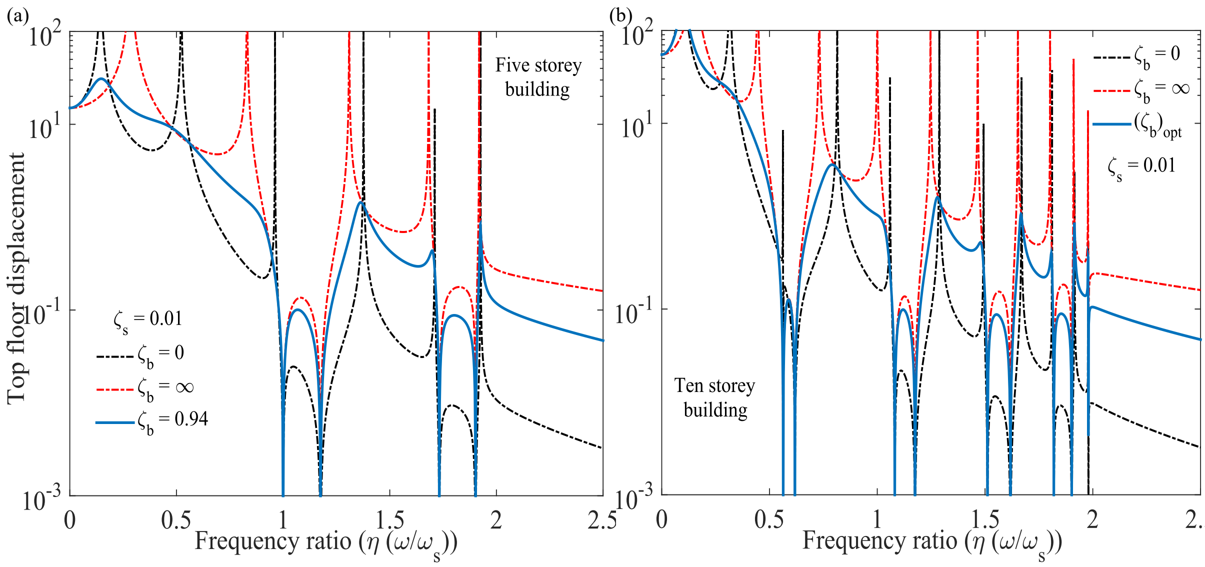

Figure 20: The variations of optimal dynamic responses of (a) five storey and (b) ten storey buildings vs frequency ratio isolated by optimum NSIABI for different values of damping ratio.

top floor of the ten storey vs frequency ratio isolated by optimum NSIABI for different values of damping ratio show in Figure 20 (b). The variations of optimal dynamic responses of the top floor of the five-storey buildings isolated by NSIABI and TBI subjected to harmonic excitation show in Figure 21 (a). The maximum dynamic responses of the top floor of the main structure have been determined as 626.83 and 30.92. Therefore, the dynamic response of the NSIABI is significantly 95.06 % superior to the traditional base isolator. The variations of optimal dynamic responses of the top floor of the ten-storey buildings isolated by NSIABI and TBI subjected to harmonic excitation show in Fig-

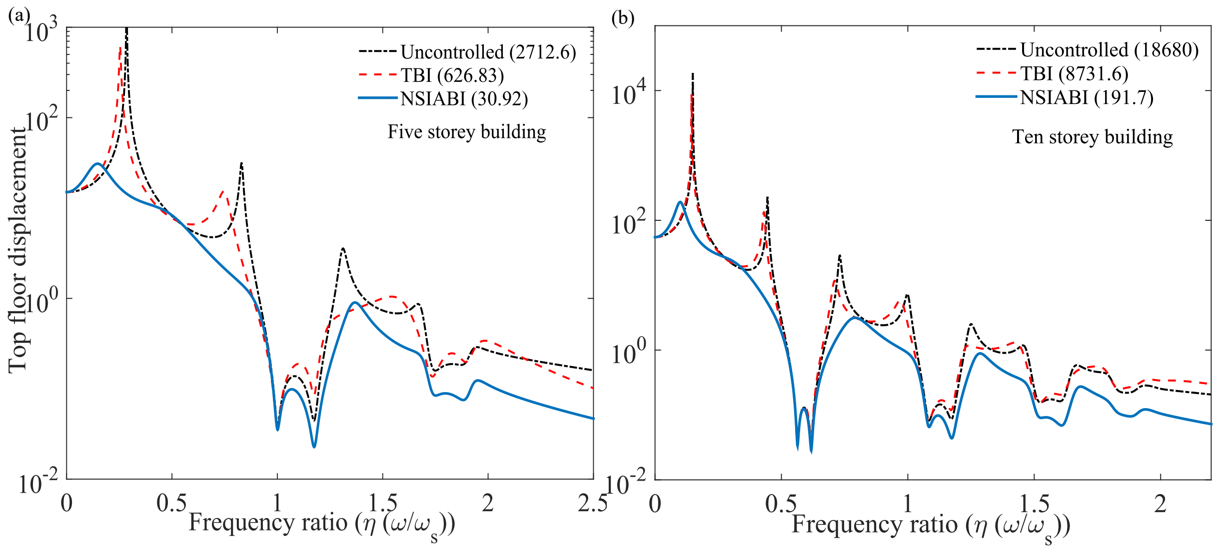

Figure 21: The variations of optimal dynamic responses of (a) five-storey and (b) ten-storey buildings isolated by NSIABI and TBI subjected to harmonic excitation.

ure 21 (b). The maximum dynamic responses of the top floor of the main structure have been determined as 8731.6 and 191.7. Therefore, the dynamic response of the NSIABI is significantly 97.80 % superior to the traditional base isolator. The variations of optimal dynamic responses of five-storey buildings isolated by NSIABI and TBI subjected to random-white noise excitation show in Figure 22 (a). The variations of optimal dynamic

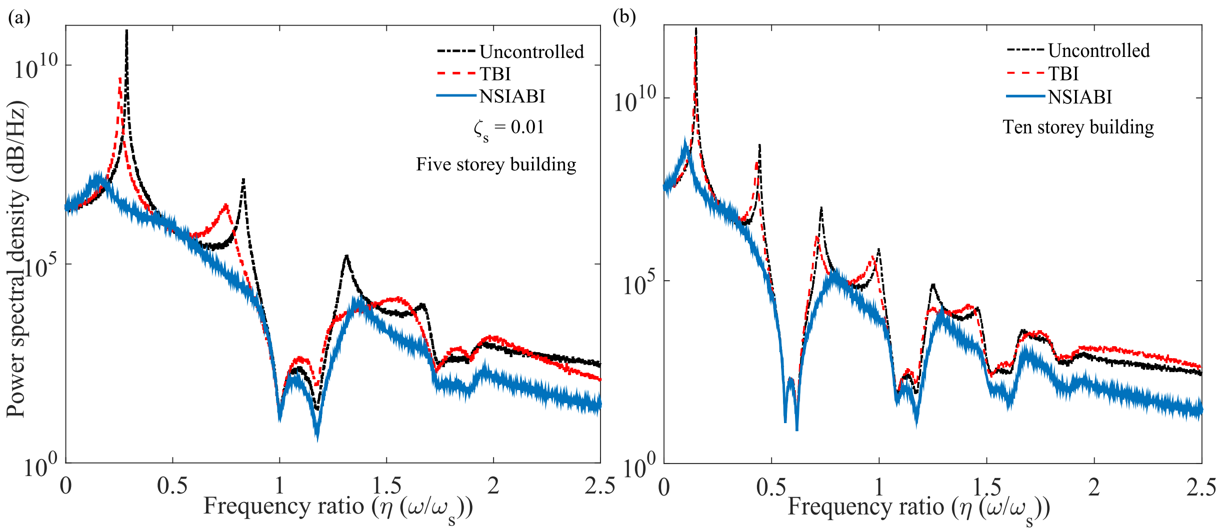

Figure 22: The variations of the optimal dynamic responses of (a) five-storey and (b) ten-storey buildings isolated by NSIABI and TBI subjected to white-noise excitation.

responses of ten-storey buildings isolated by NSIABI and TBI subjected to random-white noise excitation show in Figure 22 (b).

7. Nonlinear negative stiffness inertial amplifier base isolators for MDOF system

The nonlinear negative stiffness inertial amplifier base isolators are applied at the base of the multi-storey buildings to mitigate their dynamic responses. Therefore, Equation (38) applies to Eq. (52) and the governing equations of motion for multi-storey buildings isolated by nonlinear NSIABI subjected to base excitation are derived as

$$\begin{aligned}
&[\mathbf{M}_s]\{\ddot{\mathbf{x}}_s\} + [\mathbf{C}_s]\{\dot{\mathbf{x}}_s\} + [\mathbf{K}_s]\{\mathbf{x}_s\} = -[\mathbf{M}_s]\{\mathbf{r}\}(\ddot{x}_g + \ddot{x}_b)\\
&m_{b1}\ddot{x}_b + 2\zeta_b m_{b1}\omega_b\dot{x}_b + m_{b1}\omega_b^2 x_b - \beta m_{b1}\omega_b^2 x_b + m_{b2}x_b\ddot{x}_b + 2\zeta_b m_{b2}\omega_b x_b\dot{x}_b\\
&+ m_{b2}\omega_b^2 x_b^2 - \beta m_{b2}\omega_b^2 x_b^2 + m_{b3}x_b^2\ddot{x}_b + 2\zeta_b m_{b3}\omega_b x_b^2\dot{x}_b + m_{b3}\omega_b^2 x_b^3 - \beta m_{b3}\omega_b^2 x_b^3\\
&- k_1 x_1 - c_1\dot{x}_1 = -m_{ia}\ddot{x}_g
\end{aligned} \tag{64}$$

After applying the stochastic linearization method and Eq. (41) to the Eq. (64), the governing equations of motion for multi-storey buildings isolated by nonlinear NSIABI derive as

$$\begin{aligned}
&[\mathbf{M}_s]\{\ddot{\mathbf{x}}_s\} + [\mathbf{C}_s]\{\dot{\mathbf{x}}_s\} + [\mathbf{K}_s]\{\mathbf{x}_s\} = -[\mathbf{M}_s]\{\mathbf{r}\}(\ddot{x}_g + \ddot{x}_b)\\
&m_{b1}\ddot{x}_b + 2\zeta_b m_{b1}\omega_b\dot{x}_b + m_{b1}\omega_b^2 x_b - \beta m_{b1}\omega_b^2 x_b + 3m_{b3}\omega_b^2\sigma_{x_b}^2 x_b\\
&- 3\beta m_{b3}\omega_b^2\sigma_{x_b}^2 x_b - k_1 x_1 - c_1\dot{x}_1 = -m_{b1}\ddot{x}_g
\end{aligned} \tag{65}$$

The steady-state solutions for five storey buildings are considered as $x_1 = X_1 e^{\mathrm{i}\omega t}$, $x_2 = X_2 e^{\mathrm{i}\omega t}$, $x_3 = X_3 e^{\mathrm{i}\omega t}$, $x_4 = X_4 e^{\mathrm{i}\omega t}$, $x_5 = X_5 e^{\mathrm{i}\omega t}$, $x_b = X_b e^{\mathrm{i}\omega t}$, and $\ddot{x}_g = X_g e^{\mathrm{i}\omega t}$. Using the steady-state solutions, the transfer function derives as

$$\begin{bmatrix}
E_1 & E_2 & 0 & 0 & 0 & q^2\\
E_2 & E_1 & E_2 & 0 & 0 & q^2\\
0 & E_2 & E_1 & E_2 & 0 & q^2\\
0 & 0 & E_2 & E_1 & E_2 & q^2\\
0 & 0 & 0 & E_2 & E_3 & q^2\\
A_2 & 0 & 0 & 0 & 0 & E_4
\end{bmatrix}
\begin{Bmatrix} X_1\\ X_2\\ X_3\\ X_4\\ X_5\\ X_b \end{Bmatrix}
= -\begin{bmatrix} 1\\ 1\\ 1\\ 1\\ 1\\ \mu_{b1} \end{bmatrix} X_g \tag{66}$$

$$\begin{aligned}
&q = \mathrm{i}\omega, E_1 = 4\,\zeta_s q\omega_s + q^2 + 2\,{\omega_s}^2, E_2 = -2\,\zeta_s q\omega_s - {\omega_s}^2,\\
&E_3 = 2\,\zeta_s q\omega_s + q^2 + {\omega_s}^2, E_4 = -\mu_{b1}\eta^2 + 2\,\mathrm{i}\zeta_b\mu_{b1}\eta_b\,\eta + {\eta_b}^2\mu_{b1} - \beta{\eta_b}^2\mu_{b1} + \rho\\
&\quad \text{and} \quad \rho = 3\mu_{b3}\eta_b^2\tilde{\sigma}_{x_b}^2\,(1-\beta)
\end{aligned} \tag{67}$$

Therefore, the dynamic response of the top floor derives as

$$H_5(q) = \left(\frac{X_5}{X_g}\right)\omega_s^2 = \frac{\begin{pmatrix} (\eta^4 - 5\,\eta^2 + 5)\,(\eta - 1)\,(\eta + 1)\\ (2\,i\zeta_b\eta\,\eta_b\mu_{b1} - \beta\,{\eta_b}^2\mu_{b1} + {\eta_b}^2\mu_{b1} + \rho)\,(\eta^2 - 3) \end{pmatrix}}{\Delta} \tag{68}$$

The dynamic response of nonlinear NSIABI derives as

$$H_b(q) = \left(\frac{X_b}{X_g}\right)\omega_s^2 = \frac{\begin{pmatrix} -\eta^{10}\mu_{b1} + 9\,\eta^8\mu_{b1} + \eta^8 - 28\,\eta^6\mu_{b1} - 8\,\eta^6\\ +35\,\eta^4\mu_{b1} + 21\,\eta^4 - 15\,\mu_{b1}\eta^2 - 20\,\eta^2 + \mu_{b1} + 5 \end{pmatrix}}{\Delta} \tag{69}$$

The closed-form expression for Δ has been derived as

$$\Delta = \begin{pmatrix} \beta\,{\eta_b}^2\mu_{b1} - {\eta_b}^2\mu_{b1} + \eta^{10}{\eta_b}^2\mu_{b1} - 9\,\eta^8{\eta_b}^2\mu_{b1} - \rho + 5\,\eta^2 + 28\,\eta^6{\eta_b}^2\mu_{b1} \\ -35\,\eta^4{\eta_b}^2\mu_{b1} + 15\,\eta^2{\eta_b}^2\mu_{b1} + \mu_{b1}\eta^2 - \beta\,\eta^{10}{\eta_b}^2\mu_{b1} - 15\,\eta^4\mu_{b1} \\ +15\,\eta^2\rho - \eta^{12}\mu_{b1} + \eta^{10}\rho + 9\,\eta^{10}\mu_{b1} - 9\,\eta^8\rho - 28\,\eta^8\mu_{b1} + 28\,\eta^6\rho \\ +35\,\eta^6\mu_{b1} - 35\,\eta^4\rho - 15\,\beta\,\eta^2{\eta_b}^2\mu_{b1} - 28\,\beta\,\eta^6{\eta_b}^2\mu_{b1} + 35\,\beta\,\eta^4{\eta_b}^2\mu_{b1} \\ +9\,\beta\,\eta^8{\eta_b}^2\mu_{b1} + \eta^{10} - 8\,\eta^8 + 21\,\eta^6 - 20\,\eta^4 \\ +\mathrm{i}\begin{pmatrix} 2\,\eta^{11}\zeta_b\eta_b\mu_{b1} - 18\,\eta^9\zeta_b\eta_b\mu_{b1} + 56\,\eta^7\zeta_b\eta_b\mu_{b1} \\ -70\,\eta^5\zeta_b\eta_b\mu_{b1} + 30\,\eta^3\zeta_b\eta_b\mu_{b1} - 2\,\eta\,\zeta_b\eta_b\mu_{b1} \end{pmatrix} \end{pmatrix} \tag{70}$$

Using Eq. (69), Eq. (70), Eq. (12), and Eq. (13), $\sigma^2_{x_b}$ for multi-storey buildings derive Chowdhury et al. (2022) and expressed as

$$\sigma^2_{x_b} = \frac{S_0\pi\,\left(55\,\beta\,\mu_{b1}{\omega_b}^2 - {\omega_s}^2{\mu_{b1}}^2 - 55\,\mu_{b1}{\omega_b}^2 - 10\,\mu_{b1}{\omega_s}^2 - 25\,{\omega_s}^2\right)}{2{\mu_{b1}}^2{\omega_s}^2\zeta_b{\omega_b}^3\,(\beta-1)} \tag{71}$$

The non-dimensional form of Eq. (71) obtains as

$$\tilde{\sigma}^2_{x_b} = \left(\frac{S_0\pi}{\omega_s^3}\right)\frac{\left(55\,\beta\,\mu_{b1}{\eta_b}^2 - {\mu_{b1}}^2 - 55\,\mu_{b1}{\eta_b}^2 - 10\,\mu_{b1} - 25\,\right)}{2{\mu_{b1}}^2\zeta_b{\eta_b}^3\,(\beta-1)} \tag{72}$$

Substituting Eq. (72) and Eq. (39) to Eq. (67), ρ determines as

$$\rho = \left(\frac{3\eta_b^2(1+3\cos^2\theta)m_a}{4l^2\sin^6\theta}\right)\left(\frac{S_0\pi}{\omega_s^3}\right)\left(\frac{{\mu_{b1}}^2 + 55{\eta_b}^2\mu_{b1} + 10\,\mu_{b1} + 25 - 55\beta\,\mu_{b1}{\eta_b}^2}{2\zeta_b{\mu_{b1}}^2{\eta_b}^3}\right) \tag{73}$$

The variations of the optimal dynamic responses of five-storey buildings versus frequency ratio isolated by optimum nonlinear NSIABI show in Figure 23 (a). The variations of

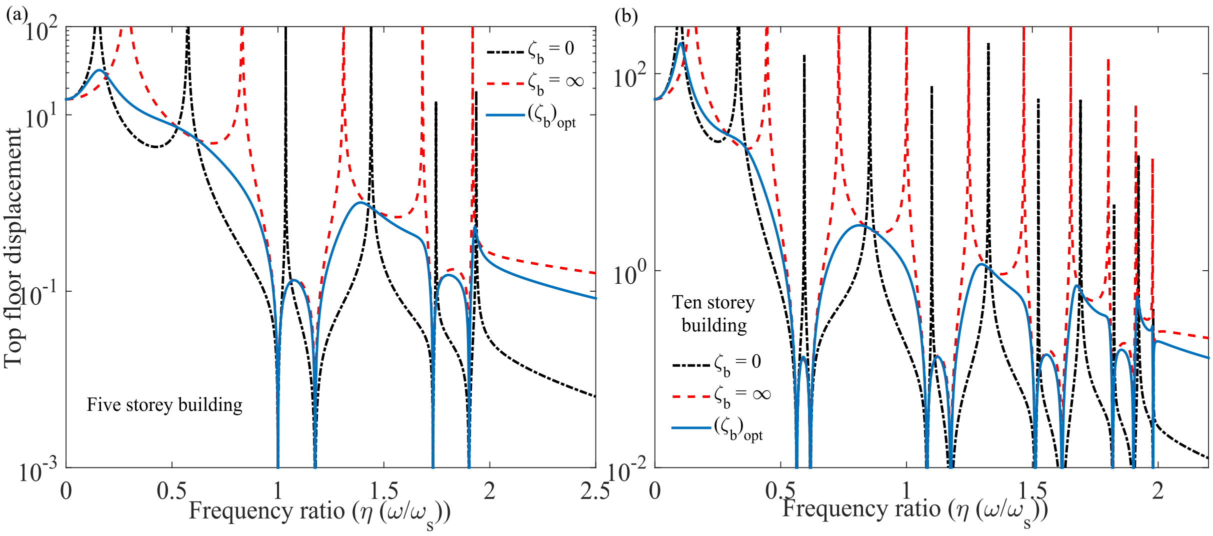

Figure 23: The variations of the optimal dynamic responses of (a) five and (b) ten-storey buildings versus frequency ratio isolated by optimum nonlinear NSIABI.

the optimal dynamic responses of ten-storey buildings versus frequency ratio isolated by optimum nonlinear NSIABI show in Figure 23 (b). The variations of the optimal dynamic responses of five-storey buildings isolated by NNSIABI and TBI subjected to harmonic excitation have been shown in Figure 24 (a). The maximum dynamic responses of the top floor of the main structure have been determined as 626.83 and 32.06. Therefore, the dynamic response of the NNSIABI is significantly 94.88 % superior to the traditional base isolator. The variations of the optimal dynamic responses of ten-storey buildings isolated

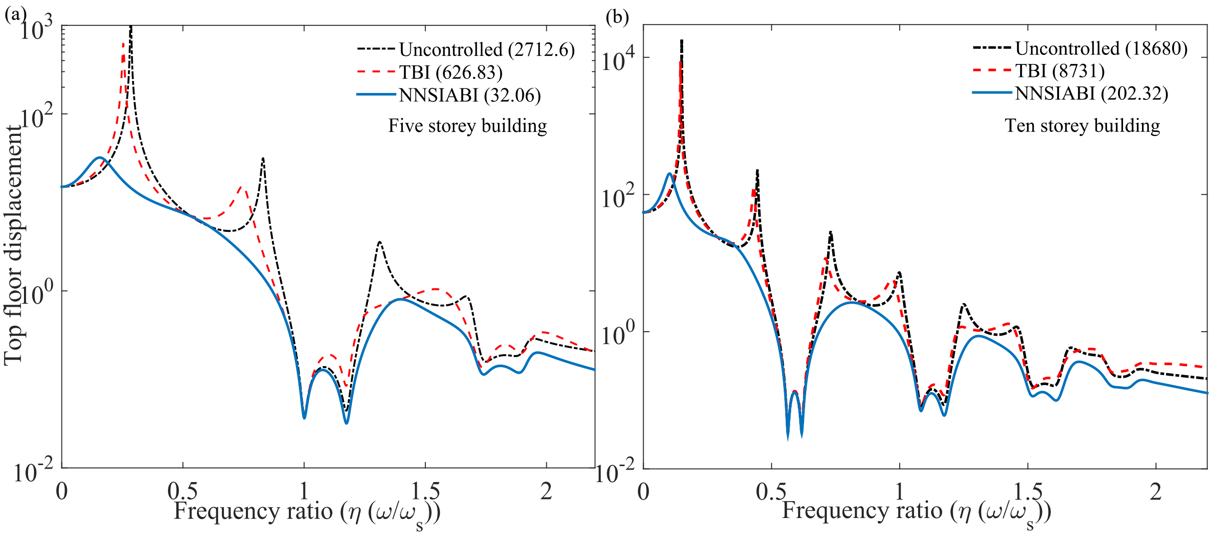

Figure 24: The variations of the optimal dynamic responses of (a) five-storey and (b) ten-storey buildings isolated by NNSIABI and TBI subjected to harmonic excitation.

by NNSIABI and TBI subjected to harmonic excitation have been shown in Figure 24 (b). The maximum dynamic responses of the top floor of the main structure have been determined as 8731 and 202.32. Therefore, the dynamic response of the NNSIABI is significantly 97.68 % superior to the traditional base isolator. The variations of the optimal dynamic responses of five-storey buildings isolated by NNSIABI and TBI subjected to random-white noise excitation show in Figure 25 (a). The maximum dynamic response of the NNSIABI-controlled main structure's are lesser than the optimum traditional base isolators. Therefore, the dynamic response reduction capacity of optimum NNSIABI is significantly higher than the optimum traditional base isolated subjected to random-white noise excitation. The variations of the optimal dynamic responses of ten-storey buildings isolated by NNSIABI and TBI subjected to random-white noise excitation show in Figure 25 (b). According to the results, the dynamic response reduction capacity of optimum NNSIABI is significantly higher than the optimum traditional base isolated subjected to random-white noise excitation for ten-storey buildings. In addition, the accuracy of the closed-form expressions for optimal design parameters for NNSIABI has been verified by conducting a numerical study. The changes in the displacement responses of the five and ten-storey buildings versus the time of the uncontrolled and isolated structures are shown in Figure 26 (a) and Figure 26 (b). The maximum displacement responses are determined for five-storey buildings and listed in Table 4. The maximum displacement responses of the main buildings and the displacement reduction capacity of NNSIABI w.r.t TBI ($D_5(\%)$) under near-field earthquake base excitations have been listed in Ta-

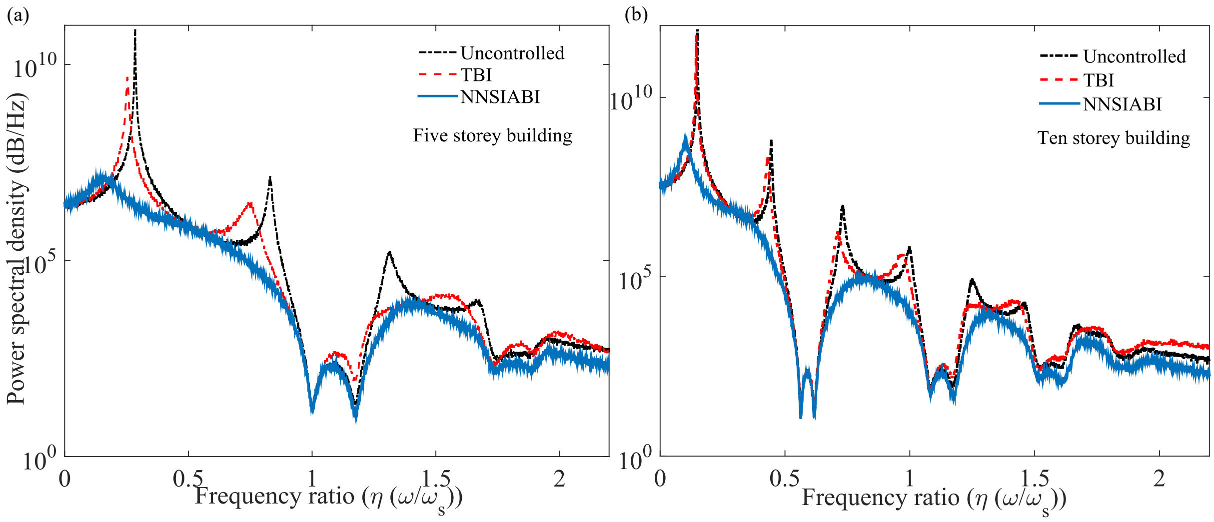

Figure 25: The variations of the optimal dynamic responses of (a) five-storey and (b) ten-storey buildings isolated by NNSIABI and TBI subjected to random-white noise excitation.

ble 4. where $(x_5^{max})_{TBI}$ refers to the maximum displacement of the multi-storey building

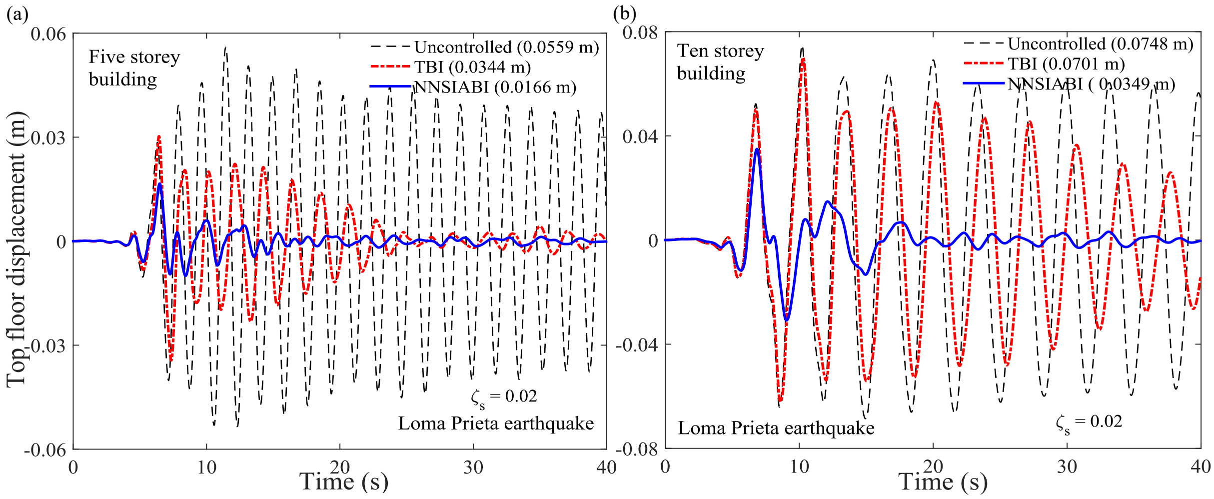

Figure 26: The displacement response of (a) five and (b) ten storey buildings vs time isolated by optimum TBI and NNSIABI subjected to Loma Prieta earthquake.

isolated by TBI. $(x_5^{max})_{NNSIABI}$ refers to the maximum displacement of the multi-storey building isolated by NNSIABI. According to this result, the proposed NNSIABI has 57.01 % more displacement reduction capacity than the traditional base isolator (TBI).

$$D_5(\%) = \frac{(x_5^{max})_{TBI} - (x_5^{max})_{NNSIABI}}{(x_5^{max})_{TBI}} \tag{74}$$

where $D_5(\%)$ defines the displacement reduction capacity of NNSIABI with respect to TBI. The changes in the acceleration responses of the five and ten-storey buildings versus the time of the uncontrolled and isolated structures are shown in Figure 27 (a) and

Figure 27 (b). The maximum acceleration responses are determined for all structures and listed in Table 5. The maximum acceleration responses of the main buildings and the displacement reduction capacity of NNSIABI w.r.t TBI ($A_5(\%)$) under near-field earthquake base excitations have been listed in Table 5.

$$A_5(\%) = \frac{(\ddot{x}_5^{max})_{TBI} - (\ddot{x}_5^{max})_{NNSIABI}}{(\ddot{x}_5^{max})_{TBI}} \tag{75}$$

According to Table 5, the NNSIABI has 54.4 % more acceleration reduction capacity

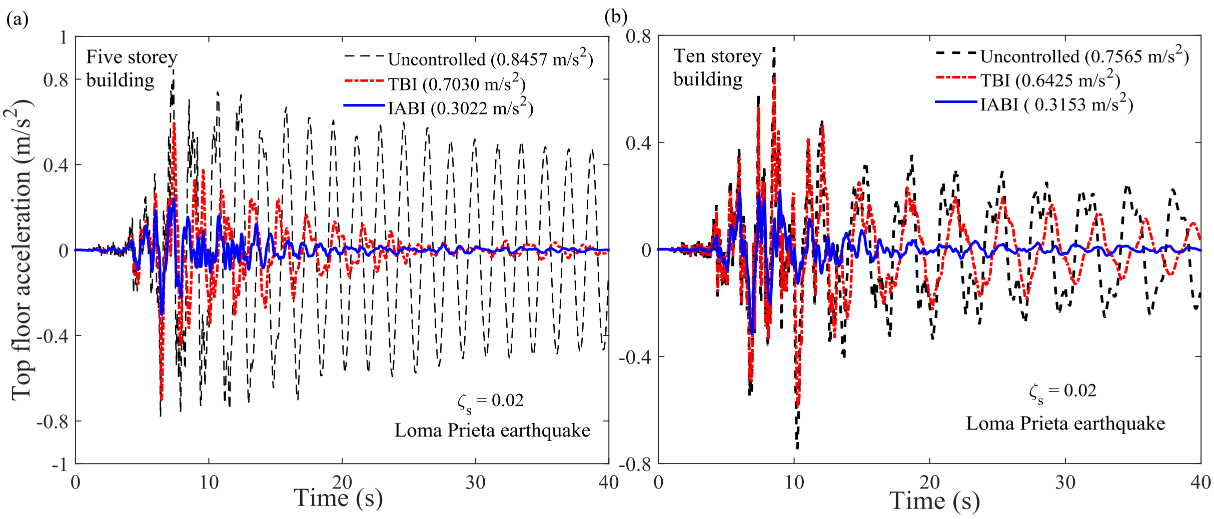

Figure 27: The acceleration response of structures vs time isolated by optimum TBI and NNSIABI subjected to Loma Prieta earthquake.

Table 4: The five-story building's maximum top floor displacement responses x_5^{max} (m) and NNSIABI's displacement reduction capability with respect to TBI ($D_5(\%)$) under near-field seismic base excitations.

Earthquake	x_5^{max} **(m)**			$D_5(\%)$
	Uncontrolled	**TBI Matsagar and Jangid (2010)**	**NNSIABI**	**NNSIABI**
Irpinia, Italy-01	0.0443	0.0305	0.0125	59.15
Superstition Hills-02	0.0469	0.0361	0.0187	48.09
Loma Prieta	0.0559	0.0344	0.0166	51.71
Erzican, Turkey	0.0678	0.0519	0.0144	72.27
Cape Mendocino	0.0317	0.03	0.0156	48.08
Landers	0.0233	0.0153	0.0074	51.86
Northridge-01	0.0913	0.0824	0.04116	50.13
Kocaeli, Turkey	0.0310	0.0155	0.0065	58.37
Chi-Chi, Taiwan	0.1310	0.0862	0.0247	71.35
Chi-Chi, Taiwan	0.0828	0.0538	0.0219	59.33
Duzce, Turkey	0.0408	0.0280	0.0121	56.77
Average	0.0588	0.0422	0.0174	57.01

than TBI for the five-storey buildings. The histogram of the uncontrolled and isolated

Table 5: The five-story structure's maximum top floor acceleration responses $\ddot{x}_5^{max}$ (m/s^2) under near-field earthquake base excitations, together with the corresponding acceleration reduction of each optimal isolator with regard to the uncontrolled building $(A_5(\%))$.

Earthquake	$\ddot{x}_5^{max}$ (m/s^2)			$A_5(\%)$
	Uncontrolled	**TBI Matsagar and Jangid (2010)**	**NNSIABI**	**NNSIABI**
Irpinia, Italy-01	0.6715	0.3592	0.1339	62.70
Superstition Hills-02	0.9009	0.7245	0.2853	60.62
Loma Prieta	0.8457	0.7030	0.3022	57.02
Erzican, Turkey	1.1287	0.9778	0.2811	71.25
Cape Mendocino	1.3075	1.2134	0.5417	55.35
Landers	0.8391	0.4476	0.2729	39.03
Northridge-01	2.0294	1.9596	1.1029	43.71
Kocaeli, Turkey	0.5715	0.2994	0.1237	58.69
Chi-Chi, Taiwan	2.253	1.204	0.5262	56.30
Chi-Chi, Taiwan	1.4161	0.6567	0.38	42.13
Duzce, Turkey	1.0875	1.0845	0.4454	58.92
Average	1.117	0.875	0.399	54.4

structures using their displacement and acceleration responses are shown in Figure 28 (a) and Figure 28 (b). The maximum dynamic responses of the isolated structures are divided by the maximum dynamic responses of the uncontrolled structures. The ratios are applied to obtain the histogram diagrams. The histogram plots of the NNSIABI-isolated structures are much smaller than the histogram diagrams of the uncontrolled structures and structures isolated by TBI. The maximum displacement responses are determined

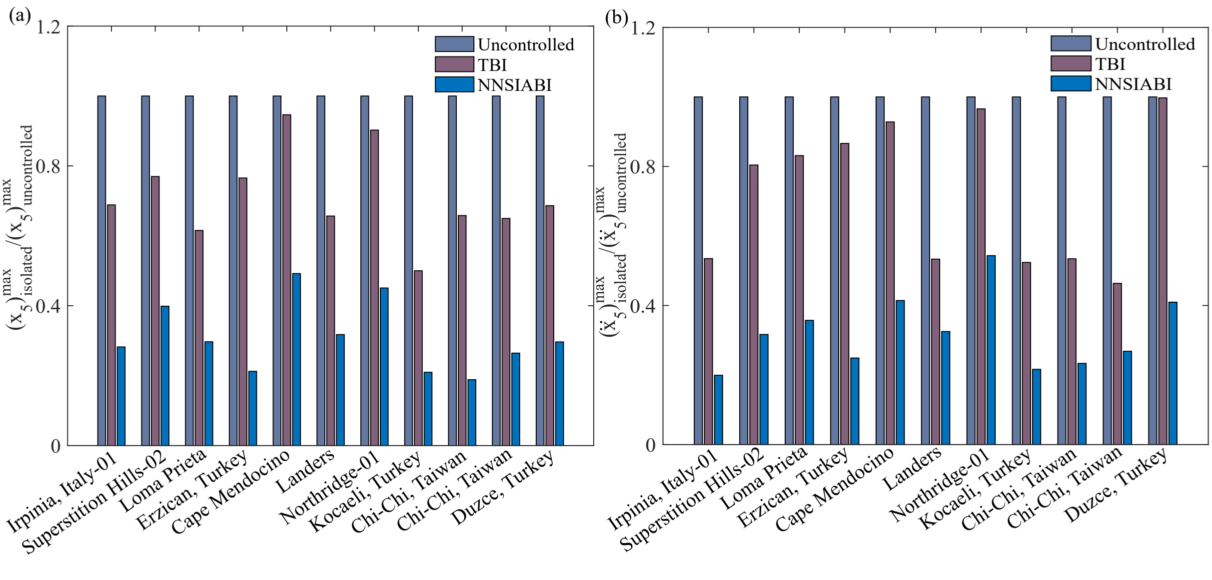

Figure 28: The bar diagrams of (a) displacement and (b) acceleration of structure isolated by TBI and NNSIABI.

for ten-storey buildings and listed in Table 6. The maximum displacement responses of the main buildings and the displacement reduction capacity of NNSIABI w.r.t TBI

$(D_{10}(\%))$ under near-field earthquake base excitations have been listed in Table 6. where

Table 6: x_{10}^{max} (m) represents the maximum top floor displacement responses of a ten-story structure, and $(D_{10}(\%))$ is the equivalent displacement reduction of each optimal isolator with respect to the uncontrolled building. Beneath base excitations for near-field earthquakes (Pulse recordings).

Earthquake	x_{10}^{max} **(m)**			$D_{10}(\%)$
	Uncontrolled	**TBI Matsagar and Jangid (2010)**	**NNSIABI**	**NNSIABI**
Irpinia, Italy-01	0.0821	0.0754	0.0329	56.36
Superstition Hills-02	0.1045	0.1025	0.0705	31.22
Loma Prieta	0.0748	0.0701	0.0349	50.15
Erzican, Turkey	0.1214	0.0997	0.0517	48.09
Cape Mendocino	0.0795	0.0674	0.0389	42.28
Landers	0.0379	0.0297	0.0115	61.23
Northridge-01	0.0766	0.0746	0.0477	36.11
Kocaeli, Turkey	0.0525	0.0509	0.0203	60.17
Chi-Chi, Taiwan	0.2109	0.1783	0.0620	65.25
Chi-Chi, Taiwan	0.1271	0.1175	0.0630	46.36
Duzce, Turkey	0.1348	0.1327	0.0545	58.93
Average	0.100	0.0907	0.044	51.48

$(x_{10}^{max})_{TBI}$ refers to the maximum displacement of the multi-storey building isolated by TBI. $(x_{10}^{max})_{NNSIABI}$ refers to the maximum displacement of the multi-storey building isolated by NNSIABI. According to this result, the proposed NNSIABI has 51.48 % more displacement reduction capacity than the traditional base isolator (TBI).

$$D_{10}(\%) = \frac{(x_{10}^{max})_{TBI} - (x_{10}^{max})_{NNSIABI}}{(x_{10}^{max})_{TBI}} \tag{76}$$

where $D_{10}(\%)$ defines the displacement reduction capacity of NNSIABI with respect to TBI. The maximum acceleration responses are determined for all structures and listed in Table 7. The maximum acceleration responses of the main buildings and the displacement reduction capacity of NNSIABI w.r.t TBI $(A_{10}(\%))$ under near-field earthquake base excitations have been listed in Table 7.

$$A_{10}(\%) = \frac{(\ddot{x}_{10}^{max})_{TBI} - (\ddot{x}_{10}^{max})_{NNSIABI}}{(\ddot{x}_{10}^{max})_{TBI}} \tag{77}$$

The histogram of the uncontrolled and isolated structures using their displacement and acceleration responses are shown in Figure 29 (a) and Figure 29 (b). The maximum dynamic responses of the isolated structures are divided by the maximum dynamic responses of the uncontrolled structures. The ratios are applied to obtain the histogram diagrams. The histogram plots of the NNSIABI-isolated structures are much smaller than the histogram diagrams of the uncontrolled structures and structures isolated by TBI. Figure 30 (a) and Figure 30 (b) show the changes in the maximum displacement and acceleration of each floor of five-story structures, both controlled and uncontrolled, that were subjected to Loma Prieta earthquake recordings with respect to floor levels. When compared to the uncontrolled structure, it is shown that TBI and NNSIABI both significantly lower the displacement and acceleration responses for each floor. In terms

Table 7: Maximum top floor acceleration responses of a ten-story structure $\ddot{x}_{10}^{max}$ (m/s^2) under near-field earthquake base excitations, with corresponding acceleration decrease of each optimal isolator with respect to the uncontrolled building ($A_{10}(\%)$).

Earthquake	$\ddot{x}_{10}^{max}$ (m/s^2)			$A_{10}(\%)$
	Uncontrolled	**TBI** Matsagar and Jangid (2010)	**NNSIABI**	**NNSIABI**
Irpinia, Italy-01	0.4515	0.4188	0.1932	53.86
Superstition Hills-02	1.1232	1.0663	0.5468	48.72
Loma Prieta	0.7565	0.6425	0.3153	50.92
Erzican, Turkey	1.0892	0.9128	0.5452	40.27
Cape Mendocino	0.9021	0.8409	0.4537	46.04
Landers	0.8337	0.5921	0.1623	72.57
Northridge-01	1.6022	1.4755	0.8028	45.59
Kocaeli, Turkey	0.3923	0.3501	0.1453	58.49
Chi-Chi, Taiwan	1.4864	1.3362	0.4686	64.93
Chi-Chi, Taiwan	0.7874	0.7245	0.3552	50.97
Duzce, Turkey	0.7617	0.6148	0.2692	56.21
Average	0.9024	0.8158	0.3851	52.79

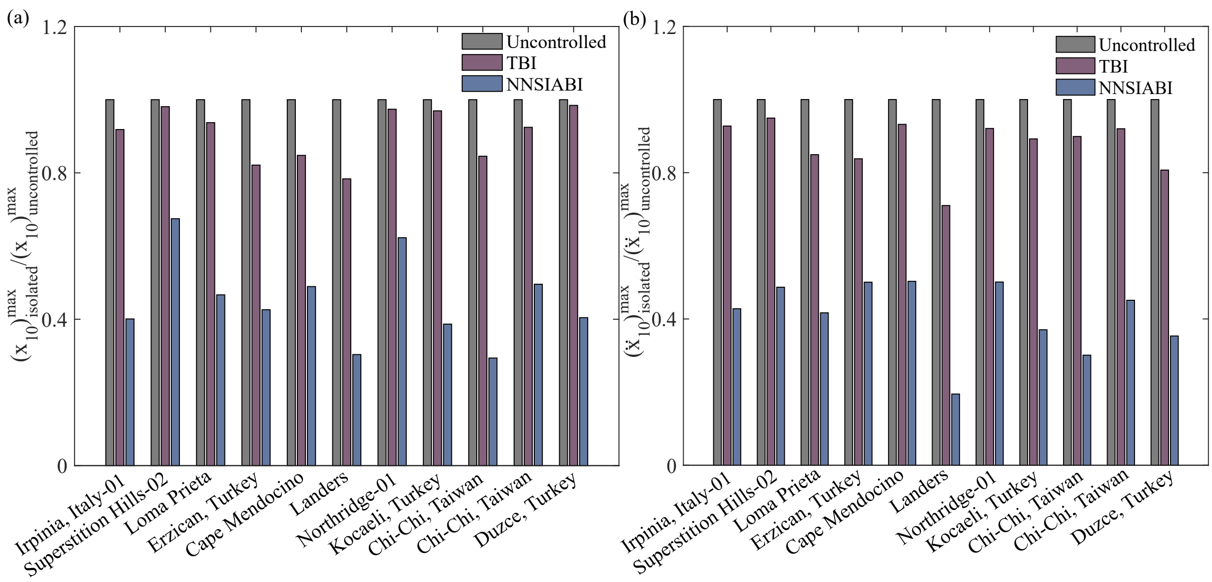

Figure 29: The bar diagrams of (a) displacement and (b) acceleration of structure isolated by TBI and NNSIABI.

552 of total floor responses, NNSIABI offers 57.01% and 54.4 % greater displacement and ac-
553 celeration reduction capabilities than TBI during near-field earthquake base excitations.
554 Figure 31 (a) and Figure 31 (b) show the changes in the maximum displacement and
555 acceleration of each floor of ten-story structures, both controlled and uncontrolled, that
556 were subjected to Loma Prieta earthquake recordings with respect to floor levels. When
557 compared to the uncontrolled structure, it is shown that TBI and NNSIABI both signifi-
558 cantly lower the displacement and acceleration responses for each floor. In terms of total
559 floor responses, NNSIABI offers 51.48% and 52.79 % greater displacement and accelera-

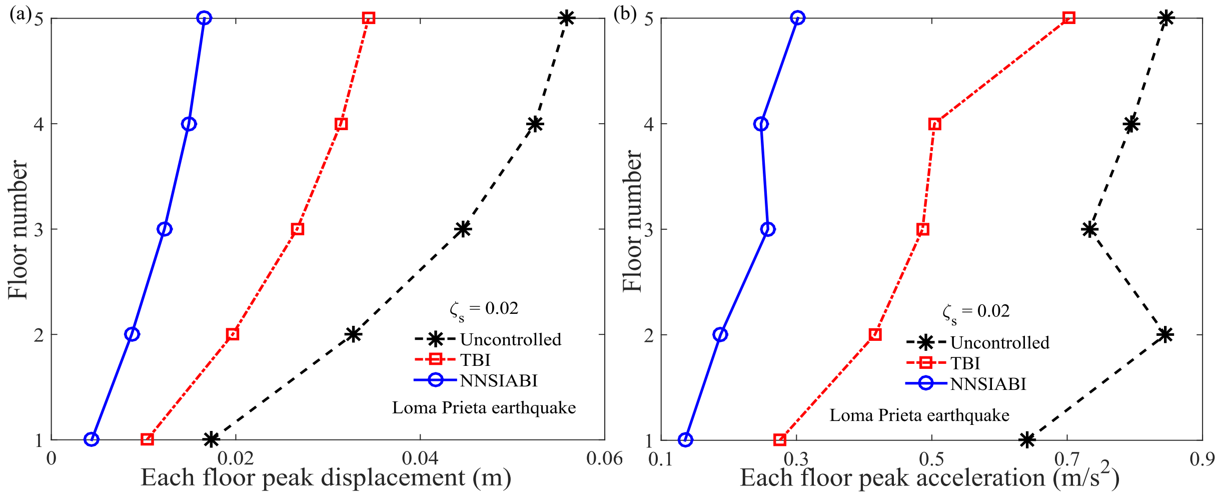

Figure 30: The variations of each floor (a) displacement and (b) acceleration of five-storey buildings isolated by TBI and NNSIABI versus floor number.

tion reduction capabilities than TBI during near-field earthquake base excitations. The

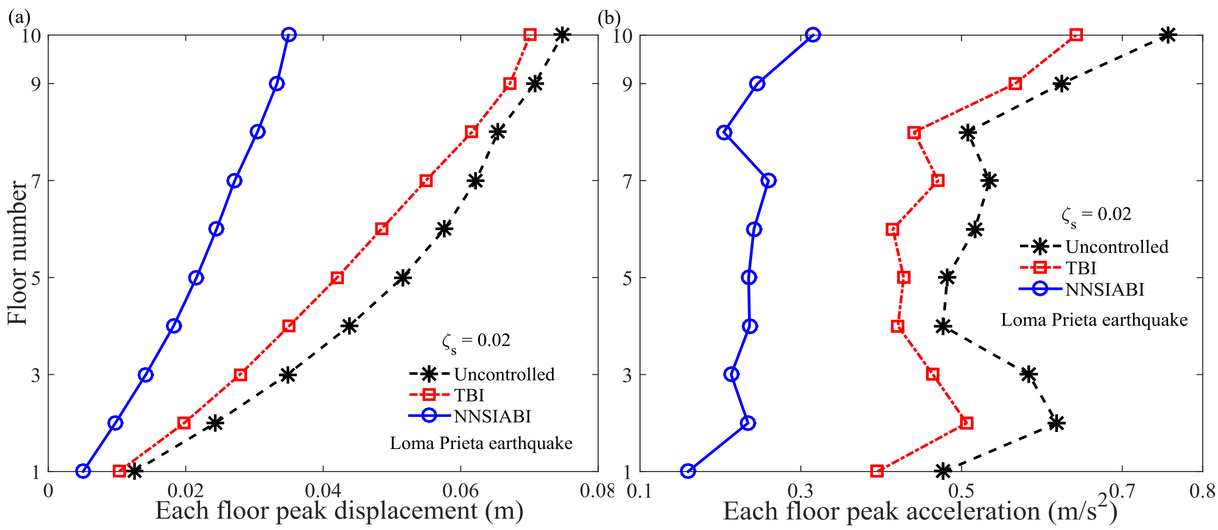

Figure 31: The variations of each floor (a) displacement and (b) acceleration of ten-storey buildings isolated by TBI and NNSIABI versus floor number.

maximum displacement of the top floor and maximum damping force of the five-story building isolated by IABI are lower than those of the uncontrolled five-story buildings, as shown by Figure 32 (a) 's hysteretic curves of the top floor damping force with viscous damping ratio of each floor ζ_s as 0.02. A similar trend has also been observed in Figure 32 (b). Figure 32 makes the damping force decrease in the NNSIABI-controlled structure very evident. In addition, the energy dissipation capacity of each isolator is obtained separately to visualise the energy flow within the structures during an earthquake. Therefore, the variations of the normalised energy of structure versus time are shown in Figure 33 (a). The kinetic energy, dissipated energy, and potential energy of

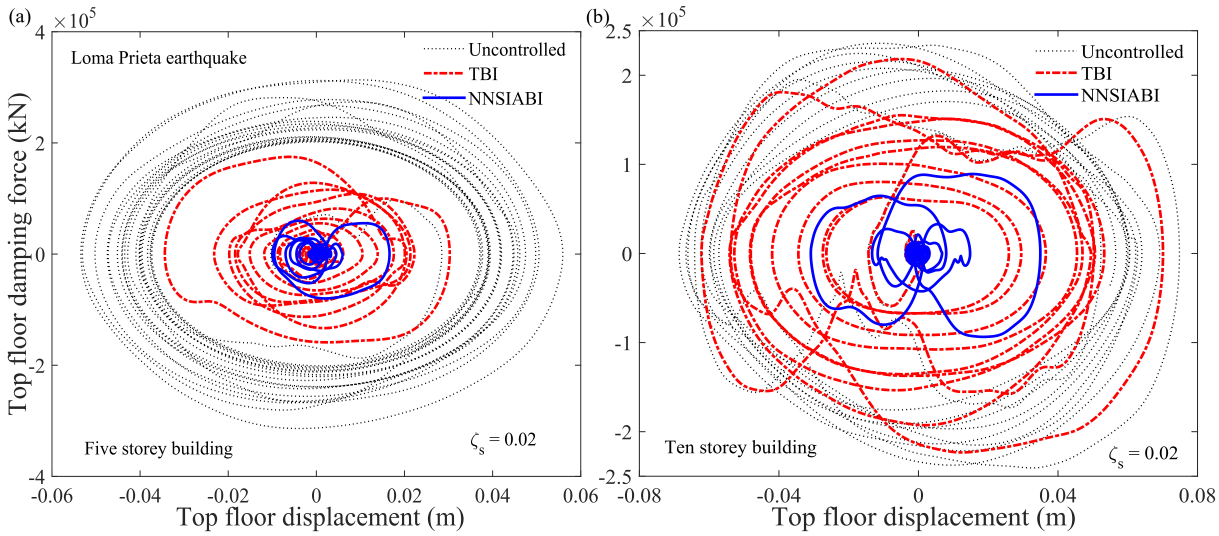

Figure 32: The variations of structural damping force versus structural displacement for (a) five and (b) ten-storey buildings.

the uncontrolled structure is obtained analytically. The potential energy is more than the dissipated and kinetic energies and has a range of 6000 to 6200. The maximum amplitudes of other energy plots are near the 800 to 900 ranges. In addition, the energy plots of each isolated structure are derived. The energy plots of each isolated structure are derived. Therefore, the variations of the normalised energy of the structures isolated by TBI and NNSIABI versus time are shown in Figure 33 (b) and Figure 33 (c). In Figure 33 (b), the potential energy plot has a maximum amplitude of 640, whereas in Figure 33 (c), the potential energy plot has a maximum amplitude of 58. The kinetic and dissipated energy plots are also following the same trends. The rest of the energy is dissipated outside the environment through mechanical energy to thermal energy during earthquake and post-earthquake scenarios. Therefore, the proposed NNSIABI is more effective than TBI in terms of vibration reduction capacity. In addition, the energy dissipation capacity of each

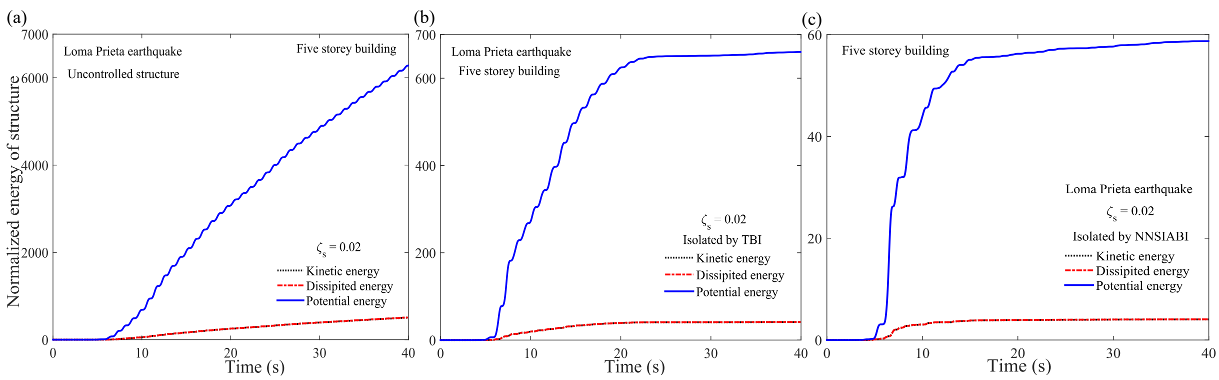

Figure 33: The variations of structural energies of five-storey buildings versus time for (a) uncontrolled structures, structures isolated by (b) TBI and (c) NNSIABI.

isolator is obtained separately to visualise the energy flow within the structures during an earthquake. Therefore, the variations of the normalised energy of structure versus time are shown in Figure 34 (a). The kinetic energy, dissipated energy, and potential energy of the uncontrolled structure is obtained analytically. The potential energy is more than the dissipated and kinetic energies and has a range of 4800. The maximum amplitudes of other energy plots are near the 40000 to 45000 ranges. In addition, the energy plots of each isolated structure are derived. The energy plots of each isolated structure are derived. Therefore, the variations of the normalised energy of the structures isolated by TBI and NNSIABI versus time are shown in Figure 34 (b) and Figure 34 (c). In Figure 34 (b), the potential energy plot has a maximum amplitude of 2500, whereas in Figure 34 (c), the potential energy plot has a maximum amplitude of 1580. The kinetic and dissipated energy plots are also following the same trends. The rest of the energy is dissipated outside the environment through mechanical energy to thermal energy during earthquake and post-earthquake scenarios. Therefore, the proposed NNSIABI is more effective than TBI in terms of vibration reduction capacity.

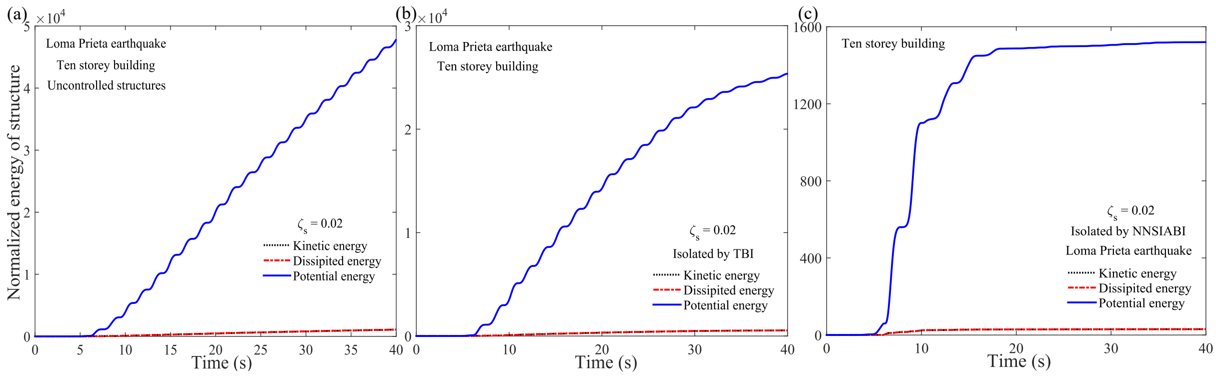

Figure 34: The variations of structural energies of ten-storey buildings versus time for (a) uncontrolled structures, structures isolated by (b) TBI and (c) NNSIABI.

8. Conclusion

This study introduces the negative stiffness inertial amplifier base isolators (NSIABI) for dynamic systems, including single- and multi-degree-of-freedom (MDOF) systems. This work also introduces the nonlinear negative stiffness inertial amplifier base isolators (NNSIABI) for dynamic systems, including single- and multi-degree-of-freedom (MDOF) systems. The exact closed-form formulas for the ideal design parameters of innovative isolators are derived using the H_2 and H_∞ optimisation techniques. For SDOF and MDOF systems exposed to harmonic and random-white noise stimulation, the dynamic response reduction capability of optimal conventional base isolators is compared to that of the H_2 and H_∞-optimized NSIABI and NNSIABI. To confirm the correctness of the H_2 and H_∞ optimised design parameters, actual earthquake records are utilised. The following is a list of the noteworthy outcomes.

- While the H_∞ optimised frequency ratio rises when the base mass ratio and amplifier's mass ratio rise, the H_2 optimised frequency ratio falls as these ratios rise.

- While the H_∞ optimised damping ratio rises when the base mass ratio and amplifier's mass ratio rise, the H_2 optimised damping ratio falls as these factors rise.

- The H_2 and H_∞ optimised NSIABI's dynamic response reduction capability for the SDOF system is notably 64.78 % and 77.14 % higher than that of the best conventional base isolator when subjected to harmonic excitations. Furthermore, H_2 and H_∞ optimised NSIABI outperform the optimal conventional base isolator when exposed to random-white noise excitations by a substantial 88 % and 94.56 %, respectively.

- The H_2 and H_∞-optimized NNSIABI's dynamic response reduction capabilities are considerably 64.66 % and 66.56 % superior to the optimal traditional base isolators for the SDOF system isolated by nonlinear negative stiffness inertial amplifier base isolators (NNSIABI).

- Placed at the base of multi-degree-of-freedom systems, including five- and ten-story structures, are the linear and nonlinear NSIABI. The findings show that the optimal linear NSIABI's dynamic response reduction capabilities are much higher than the optimum conventional base isolators for five and ten-story structures, at 95.06 % and 97.80 %, respectively.

- Furthermore, the best nonlinear negative stiffness inertial amplifier base isolators (NNSIABI) are 94.88% and 97.68% better than the conventional base isolators for five and ten-story structures, respectively.

- The real earthquake records are applied. According to that, the proposed NNSIABI has 23.42 % and 29.48 % more displacement and acceleration reduction capacities than TBI when applied to the SDOF systems.

- For the five-storey buildings, the proposed NNSIABI has 57.01 % and 54.4 % more displacement and acceleration reduction capacities than TBI. In addition, for ten-storey buildings, the proposed NNSIABI has 51.48 % and 52.79 % more displacement and acceleration reduction capacities than TBI.

- The outcomes demonstrate how effective IABI is in lowering the near-field earthquake base excitation pulse records. Traditional base isolators' ability to reduce vibration declines noticeably as floor levels in multi-story structures rise, mainly over ten stories. NNSIABI nonetheless effectively reduces acceleration and displacement responses. Additionally successful is NNSIABI's damping force decrease. NNSIABI continues to work after ten stories.

To the best of the author's knowledge, the uniqueness of the study is the introduction of linear and nonlinear negative stiffness inertial amplifier base isolators, which have not been reported in any state of the art. The recently developed mathematical formulas for the ideal design parameters of innovative dampers are further noteworthy contributions. These mathematical formulas provide the innovative isolators with an ideal design, which leads to a strong dynamic reduction capacity for the structures. The use of these innovative isolators for the dynamic response mitigation of nonlinear single- and multi-degree-of-freedom systems will be the future focus of the research.

ORCID ID

Sudip Chowdhury: https://orcid.org/0000-0001-6218-4843
Arnab Banerjee: https://orcid.org/0000-0002-3157-6200

Sondipon Adhikari: http://orcid.org/0000-0003-4181-3457

Declaration of competing interest

The authors declare that they have no known competing financial interests or personal relationships that could have appeared to influence the work reported in this paper

Data Availability Statement

All data, models, and code generated or used during the study appear in the submitted article.

Acknowledgement

The authors would like to acknowledge the Inspire faculty grant, grant number DST/ INSPIRE/04/2018/000052, for partial financial support for the project. SC would like to acknowledge the MHRD grant received from IIT Delhi during the period of this research work. SC also would like to acknowledge the IRD Early-Doc Fellowship received from IIT Delhi during the period of this research work.

References

Abalı, E., and Uckan, E. (2010). Parametric analysis of liquid storage tanks base isolated by curved surface sliding bearings. *Soil Dynamics and Earthquake Engineering*, *30*, 21–31.

Ahmad, S., Ghani, F., and Adil, M. R. (2009). Seismic friction base isolation performance using demolished waste in masonry housing. *Construction and Building Materials*, *23*, 146–152.

Allen, J. C. (2012). *H_∞ Engineering and Amplifier Optimization*. Springer Science & Business Media.

Aly, A. A., and Salem, F. A. (2013). Vehicle suspension systems control: a review. *International journal of control, automation and systems*, *2*, 46–54.

Asami, T., Nishihara, O., and Baz, A. M. (2002). Analytical solutions to h_∞ and h_2 optimization of dynamic vibration absorbers attached to damped linear systems. *J. Vib. Acoust.*, *124*, 284–295.

Ayad, M., Karathanasopoulos, N., Ganghoffer, J.-F., and Lakiss, H. (2020a). Higher-gradient and micro-inertia contributions on the mechanical response of composite beam structures. *International Journal of Engineering Science*, *154*, 103318.

Ayad, M., Karathanasopoulos, N., Reda, H., Ganghoffer, J.-F., and Lakiss, H. (2020b). On the role of second gradient constitutive parameters in the static and dynamic analysis of heterogeneous media with micro-inertia effects. *International Journal of Solids and Structures*, *190*, 58–75.

Baduidana, M., and Kenfack-Jiotsa, A. (2021). Optimal design of inerter-based isolators minimizing the compliance and mobility transfer function versus harmonic and random ground acceleration excitation. *Journal of Vibration and control*, *27*, 1297–1310.

Bai, X.-X., Jiang, P., and Qian, L.-J. (2017). Integrated semi-active seat suspension for both longitudinal and vertical vibration isolation. *Journal of Intelligent Material Systems and Structures*, *28*, 1036–1049.

Banerjee, A., Chanda, A., and Das, R. (2017). Seismic analysis of a curved bridge considering deck-abutment pounding interaction: an analytical investigation on the post-impact response. *Earthquake Engineering & Structural Dynamics*, *46*, 267–290.

Barys, M., Jensen, J. S., and Frandsen, N. M. (2018). Efficient attenuation of beam vibrations by inertial amplification. *European Journal of Mechanics-A/Solids*, *71*, 245–257.

Barys, M., and Zalewski, R. (2018). Analysis of inertial amplification mechanism with smart spring-damper for attenuation of beam vibrations. In *MATEC Web of Conferences* (p. 03002). EDP Sciences volume 157.

Buckle, I. G. (1985). New zealand seismic base isolation concepts and their application to nuclear engineering. *Nuclear Engineering and Design*, *84*, 313–326.

Čakmak, D., Tomičević, Z., Wolf, H., Božić, Ž., and Semenski, D. (2021). Stability and performance of supercritical inerter-based active vibration isolation systems. *Journal of Sound and Vibration*, (p. 116234).

Čakmak, D., Tomičević, Z., Wolf, H., Božić, Ž., and Semenski, D. (2022). Stability and performance of supercritical inerter-based active vibration isolation systems. *Journal of Sound and Vibration*, *518*, 116234.

Carrella, A., Brennan, M., Kovacic, I., and Waters, T. (2009). On the force transmissibility of a vibration isolator with quasi-zero-stiffness. *Journal of Sound and Vibration*, *322*, 707–717.

Carrella, A., Brennan, M., and Waters, T. (2007). Static analysis of a passive vibration isolator with quasi-zero-stiffness characteristic. *Journal of sound and vibration*, *301*, 678–689.

Chen, M. Z., and Hu, Y. (2019). *Inerter and Its Application in Vibration Control Systems*. Springer.

Cheng, C., Li, S., Wang, Y., and Jiang, X. (2016). On the analysis of a high-static-low-dynamic stiffness vibration isolator with time-delayed cubic displacement feedback. *Journal of Sound and Vibration*, *378*, 76–91.

Cheng, X., Jing, W., and Gong, L. (2017). Simplified model and energy dissipation characteristics of a rectangular liquid-storage structure controlled with sliding base isolation and displacement-limiting devices. *Journal of Performance of Constructed Facilities*, *31*, 04017071.

Cheng, Z., Palermo, A., Shi, Z., and Marzani, A. (2020). Enhanced tuned mass damper using an inertial amplification mechanism. *Journal of Sound and Vibration*, (p. 115267).

Cheung, Y., and Wong, W. O. (2011). h_∞ optimization of a variant design of the dynamic vibration absorber—revisited and new results. *Journal of Sound and Vibration*, *330*, 3901–3912.

Chopra, A. K. (2007). *Dynamics of structures*. Pearson Education India.

Chowdhury, S., and Banerjee, A. (2022). The exact closed-form expressions for optimal design parameters of resonating base isolators. *International Journal of Mechanical Sciences*, *224*, 107284.

Chowdhury, S., Banerjee, A., and Adhikari, S. (0). Optimal design of inertial amplifier base isolators for dynamic response control of multi-storey buildings. *International Journal of Structural Stability and Dynamics*, *0*, null. URL: https://doi.org/10.1142/S0219455423500475. doi:10.1142/S0219455423500475. arXiv:https://doi.org/10.1142/S0219455423500475.

Chowdhury, S., Banerjee, A., and Adhikari, S. (2021). Enhanced seismic base isolation using inertial amplifiers. *Structures*, *33*, 1340–1353. URL: https://www.sciencedirect.com/science/article/pii/S2352012421003908. doi:https://doi.org/10.1016/j.istruc.2021.04.089.

Chowdhury, S., Banerjee, A., and Adhikari, S. (2022). Optimal negative stiffness inertial-amplifier-base-isolators: Exact closed-form expressions. *International Journal of Mechanical Sciences*, (p. 107044).

Chun, S., Lee, Y., and Kim, T.-H. (2015). h_∞ optimization of dynamic vibration absorber variant for vibration control of damped linear systems. *journal of sound and vibration*, *335*, 55–65.

Crandall, S. H., and Mark, W. D. (2014). *Random vibration in mechanical systems*. Academic Press.

De Domenico, D., Deastra, P., Ricciardi, G., Sims, N. D., and Wagg, D. J. (2019). Novel fluid inerter based tuned mass dampers for optimised structural control of base-isolated buildings. *Journal of the Franklin Institute*, *356*, 7626–7649.

Den Hartog, J. P. (1985). *Mechanical vibrations*. Courier Corporation.

Du, H., Li, W., and Zhang, N. (2011). Semi-active variable stiffness vibration control of vehicle seat suspension using an mr elastomer isolator. *Smart materials and structures*, *20*, 105003.

Ebrahimi, B., Bolandhemmat, H., Khamesee, M. B., and Golnaraghi, F. (2011). A hybrid electromagnetic shock absorber for active vehicle suspension systems. *Vehicle System Dynamics*, *49*, 311–332.

Frandsen, N. M., Bilal, O. R., Jensen, J. S., and Hussein, M. I. (2016). Inertial amplification of continuous structures: Large band gaps from small masses. *Journal of Applied Physics*, *119*, 124902.

Fulcher, B. A., Shahan, D. W., Haberman, M. R., Conner Seepersad, C., and Wilson, P. S. (2014). Analytical and experimental investigation of buckled beams as negative stiffness elements for passive vibration and shock isolation systems. *Journal of Vibration and Acoustics*, *136*.

Furinghetti, M., Lanese, I., and Pavese, A. (2020). Experimental assessment of the seismic response of a base-isolated building through a hybrid simulation. *Recent Advances and Applications of Seismic Isolation and Energy Dissipation Devices*, .

Furinghetti, M., Pavese, A., Quaglini, V., and Dubini, P. (2019). Experimental investigation of the cyclic response of double curved surface sliders subjected to radial and bidirectional sliding motions. *Soil Dynamics and Earthquake Engineering*, *117*, 190–202.

Furinghetti, M., Yang, T., Calvi, P. M., and Pavese, A. (2021). Experimental evaluation of extra-stroke displacement capacity for curved surface slider devices. *Soil Dynamics and Earthquake Engineering*, *146*, 106752.

Han, C., Kang, B.-H., Choi, S.-B., Tak, J. M., and Hwang, J.-H. (2019). Control of landing efficiency of an aircraft landing gear system with magnetorheological dampers. *Journal of Aircraft*, *56*, 1980–1986.

Hao, Z., and Cao, Q. (2015). The isolation characteristics of an archetypal dynamical model with stable-quasi-zero-stiffness. *Journal of sound and vibration*, *340*, 61–79.

de Haro Moraes, F., Silveira, M., and Gonçalves, P. J. P. (2018). On the dynamics of a vibration isolator with geometrically nonlinear inerter. *Nonlinear Dynamics*, *93*, 1325–1340.

Hou, M., Wu, J. H., Cao, S., Guan, D., and Zhu, Y. (2017). Extremely low frequency band gaps of beam-like inertial amplification metamaterials. *Modern Physics Letters B*, *31*, 1750251.

Hu, Y., and Chen, M. Z. (2015). Performance evaluation for inerter-based dynamic vibration absorbers. *International Journal of Mechanical Sciences*, *99*, 297–307.

Hua, Y., Wong, W., and Cheng, L. (2018). Optimal design of a beam-based dynamic vibration absorber using fixed-points theory. *Journal of Sound and Vibration*, *421*, 111–131.

Huang, X., Liu, X., Sun, J., Zhang, Z., and Hua, H. (2014). Vibration isolation characteristics of a nonlinear isolator using euler buckled beam as negative stiffness corrector: a theoretical and experimental study. *Journal of Sound and Vibration*, *333*, 1132–1148.

Hwang, J., and Chiou, J. (1996). An equivalent linear model of lead-rubber seismic isolation bearings. *Engineering Structures*, *18*, 528–536.

Iemura, H., Igarashi, A., Pradono, M. H., and Kalantari, A. (2006). Negative stiffness friction damping for seismically isolated structures. *Structural Control and Health Monitoring: The Official Journal of the International Association for Structural Control and Monitoring and of the European Association for the Control of Structures*, *13*, 775–791.

Iemura, H., and Pradono, M. H. (2009). Advances in the development of pseudo-negative-stiffness dampers for seismic response control. *Structural Control and Health Monitoring: The Official Journal of the International Association for Structural Control and Monitoring and of the European Association for the Control of Structures*, *16*, 784–799.

Jangid, R. (2005a). Computational numerical models for seismic response of structures isolated by sliding systems. *Structural Control and Health Monitoring*, *12*, 117–137.

Jangid, R. (2005b). Optimum friction pendulum system for near-fault motions. *Engineering Structures*, *27*, 349–359.

Jangid, R. (2007). Optimum lead–rubber isolation bearings for near-fault motions. *Engineering Structures*, *29*, 2503–2513.

Jiang, Y., Zhao, Z., Zhang, R., De Domenico, D., and Pan, C. (2020). Optimal design based on analytical solution for storage tank with inerter isolation system. *Soil Dynamics and Earthquake Engineering*, *129*, 105924.

Kapasakalis, K. A., Antoniadis, I. A., and Sapountzakis, E. J. (2020). Performance assessment of the kdamper as a seismic absorption base. *Structural Control and Health Monitoring*, *27*, e2482.

Kapasakalis, K. A., Antoniadis, I. A., and Sapountzakis, E. J. (2021). Constrained optimal design of seismic base absorbers based on an extended kdamper concept. *Engineering Structures*, *226*, 111312.

Karathanasopoulos, N., Dos Reis, F., Diamantopoulou, M., and Ganghoffer, J.-F. (2020). Mechanics of beams made from chiral metamaterials: Tuning deflections through normal-shear strain couplings. *Materials & Design*, *189*, 108520.

Kazeminezhad, E., Kazemi, M. T., and Mirhosseini, S. M. (2020). Assessment of the vertical stiffness of elastomeric bearing due to displacement and rotation. *International Journal of Non-Linear Mechanics*, *119*, 103306.

Kuhnert, W. M., Gonçalves, P. J. P., Ledezma-Ramirez, D. F., and Brennan, M. J. (2020). Inerter-like devices used for vibration isolation: A historical perspective. *Journal of the Franklin Institute*, .

Lakes, R. S., Lee, T., Bersie, A., and Wang, Y.-C. (2001). Extreme damping in composite materials with negative-stiffness inclusions. *Nature*, *410*, 565–567.

Li, J.-Y., Lu, J., and Zhou, H. (2023). Reliability analysis of structures with inerter-based isolation layer under stochastic seismic excitations. *Reliability Engineering & System Safety*, *235*, 109222.

Li, M., Cheng, W., and Xie, R. (2021). A quasi-zero-stiffness vibration isolator using a cam mechanism with user-defined profile. *International Journal of Mechanical Sciences*, *189*, 105938.

Lindberg, E., Östberg, M., Hörlin, N.-E., and Göransson, P. (2014). A vibro-acoustic reduced order model using undeformed coupling interface substructuring–application to rubber bushing isolation in vehicle suspension systems. *Applied acoustics*, *78*, 43–50.

Liu, X., Huang, X., and Hua, H. (2013). On the characteristics of a quasi-zero stiffness isolator using euler buckled beam as negative stiffness corrector. *Journal of Sound and Vibration*, *332*, 3359–3376.

Matsagar, V., and Jangid, R. (2010). Impact response of torsionally coupled base-isolated structures. *Journal of vibration and control*, *16*, 1623–1649.

Matsagar, V. A., and Jangid, R. (2003). Seismic response of base-isolated structures during impact with adjacent structures. *Engineering Structures*, *25*, 1311–1323.

Matsagar, V. A., and Jangid, R. (2004). Influence of isolator characteristics on the response of base-isolated structures. *Engineering structures*, *26*, 1735–1749.

Mazza, F. (2019). Effects of the long-term behaviour of isolation devices on the seismic response of base-isolated buildings. *Structural Control and Health Monitoring*, *26*, e2331.

Miniaci, M., Mazzotti, M., Amendola, A., and Fraternali, F. (2020). Inducing dispersion curves with negative group velocity in inertially amplified phononic crystals through the application of an external state of prestress. In *XI International Conference on Structural Dynamic, EURODYN 2020* (pp. 612–620).

Moghimi, G., and Makris, N. (2020). Seismic response of yielding structures equipped with inerters. *Soil Dynamics and Earthquake Engineering*, (p. 106474).

Muhammad, S., Wang, S., Li, F., and Zhang, C. (2020). Bandgap enhancement of periodic nonuniform metamaterial beams with inertial amplification mechanisms. *Journal of Vibration and Control*, (p. 1077546319895630).

Nguyen, X. B., Komatsuzaki, T., and Truong, H. T. (2022). Adaptive parameter identification of bouc-wen hysteresis model for a vibration system using magnetorheological elastomer. *International Journal of Mechanical Sciences*, *213*, 106848.

Ong, P. P., Adnan, A., Kwok, K. C., Ma, C.-K., Tiong, P., and Behbahani, H. P. (2017). Dynamic simulation of unrestrained interlocking tuned liquid damper blocks. *Construction and Building Materials*, *144*, 586–597.

Palazzo, B., and Petti, L. (1999). Optimal structural control in the frequency domain: control in norm h_∞ and h_2. *Journal of Structural Control*, *6*, 205–221.

Pasala, D., Sarlis, A., Nagarajaiah, S., Reinhorn, A., Constantinou, M., and Taylor, D. (2013). Adaptive negative stiffness: new structural modification approach for seismic protection. *Journal of structural Engineering*, *139*, 1112–1123.

Peng, Y., Ma, Y., Huang, T., and De Domenico, D. (2021). Reliability-based design optimization of adaptive sliding base isolation system for improving seismic performance of structures. *Reliability Engineering & System Safety*, *205*, 107167.

Qian, F., Luo, Y., Sun, H., Tai, W. C., and Zuo, L. (2019a). Optimal tuned inerter dampers for performance enhancement of vibration isolation. *Engineering Structures*, *198*, 109464.

Qian, F., Luo Sr, Y., Sun, H., Tai, W. C., and Zuo, L. (2019b). Performance enhancement of a base-isolation structure using optimal tuned inerter dampers. In *Active and Passive Smart Structures and Integrated Systems XIII* (p. 1096715). International Society for Optics and Photonics volume 10967.

Roberts, J. B., and Spanos, P. D. (2003). *Random vibration and statistical linearization*. Courier Corporation.

Robertson, W. S., Kidner, M., Cazzolato, B. S., and Zander, A. C. (2009). Theoretical design parameters for a quasi-zero stiffness magnetic spring for vibration isolation. *Journal of Sound and Vibration*, *326*, 88–103.

Robinson, W. H. (1982). Lead-rubber hysteretic bearings suitable for protecting structures during earthquakes. *Earthquake engineering & structural dynamics*, *10*, 593–604.

Sarlis, A., Pasala, D., Constantinou, M. C., Reinhorn, A. M., Nagarajaiah, S., and Taylor, D. P. (2016). Negative stiffness device for seismic protection of structures: shake table testing of a seismically isolated structure. *Journal of Structural Engineering*, *142*, 04016005.

Sarlis, A. A., Pasala, D. T. R., Constantinou, M., Reinhorn, A., Nagarajaiah, S., and Taylor, D. (2013). Negative stiffness device for seismic protection of structures. *Journal of Structural Engineering*, *139*, 1124–1133.

Shakib, H., and Fuladgar, A. (2003). Response of pure-friction sliding structures to three components of earthquake excitation. *Computers & Structures*, *81*, 189–196.

Sheng, T., Liu, G.-b., Bian, X.-c., Shi, W.-x., and Chen, Y. (2022). Development of a three-directional vibration isolator for buildings subject to metro-and earthquake-induced vibrations. *Engineering Structures*, *252*, 113576.

Shi, X., and Zhu, S. (2017). Simulation and optimization of magnetic negative stiffness dampers. *Sensors and Actuators A: Physical*, *259*, 14–33.

Sierra, I. E. M., Losanno, D., Strano, S., Marulanda, J., and Thomson, P. (2019). Development and experimental behavior of hdr seismic isolators for low-rise residential buildings. *Engineering Structures*, *183*, 894–906.

Smith, M. C., and Wang, F.-C. (2004). Performance benefits in passive vehicle suspensions employing inerters. *Vehicle system dynamics*, *42*, 235–257.

Sun, F., Dai, X., Liu, Y., and Xiao, L. (2021). Seismic mitigation performance of periodic foundations with inertial amplification mechanism considering superstructure-foundation interaction. *Smart Materials and Structures*, *30*, 025018.

Sun, H., Zuo, L., Wang, X., Peng, J., and Wang, W. (2019). Exact h2 optimal solutions to inerter-based isolation systems for building structures. *Structural Control and Health Monitoring*, *26*, e2357.

Taniker, S., and Yilmaz, C. (2013). Phononic gaps induced by inertial amplification in bcc and fcc lattices. *Physics Letters A*, *377*, 1930–1936.

Taniker, S., and Yilmaz, C. (2017). Generating ultra wide vibration stop bands by a novel inertial amplification mechanism topology with flexure hinges. *International Journal of Solids and Structures*, *106*, 129–138.

Touaillon, J. (1870). Improvement in buildings. U.S. Patent No. 99,973.

Toygar, O., Ulgen, D., and Fidan, N. B. (2022). Assessing vibration isolation performance of single and coupled wave barriers through field experiments. *Construction and Building Materials*, *354*, 129156.

Tubaldi, E., Mitoulis, S. A., and Ahmadi, H. (2018). Comparison of different models for high damping rubber bearings in seismically isolated bridges. *Soil Dynamics and Earthquake Engineering*, *104*, 329–345.

Wang, F.-C., Liao, M.-K., Liao, B.-H., Su, W.-J., and Chan, H.-A. (2009). The performance improvements of train suspension systems with mechanical networks employing inerters. *Vehicle System Dynamics*, *47*, 805–830.

Wang, M., Sun, F.-f., and Jin, H.-j. (2018). Performance evaluation of existing isolated buildings with supplemental passive pseudo-negative stiffness devices. *Engineering Structures*, *177*, 30–46.

Wang, M., Sun, F.-F., Koetaka, Y., Chen, L., Nagarajaiah, S., and Du, X.-L. (2023). Frequency independent damped outrigger systems for multi-mode seismic control of super tall buildings with frequency independent negative stiffness enhancement. *Earthquake Engineering & Structural Dynamics*, .

Wang, M., Sun, F.-f., and Nagarajaiah, S. (2019a). Simplified optimal design of mdof structures with negative stiffness amplifying dampers based on effective damping. *The Structural Design of Tall and Special Buildings*, *28*, e1664.

Wang, M., Sun, F.-F., Nagarajaiah, S., and Li, Y.-W. (2022). Frequency-dependency/independency analysis of damping magnification effect provided by tuned inerter absorber and negative stiffness amplifying damper considering soil-structure interaction. *Mechanical Systems and Signal Processing*, *172*, 108965.

Wang, M., Sun, F.-f., Yang, J.-q., and Nagarajaiah, S. (2019b). Seismic protection of sdof systems with a negative stiffness amplifying damper. *Engineering Structures*, *190*, 128–141.

Wei, X., Lui, H., and Qin, Y. (2011). Fault isolation of rail vehicle suspension systems by using similarity measure. In *Proceedings of 2011 IEEE International Conference on Service Operations, Logistics and Informatics* (pp. 391–396). IEEE.

Winterflood, J., Blair, D. G., and Slagmolen, B. (2002). High performance vibration isolation using springs in euler column buckling mode. *Physics Letters A*, *300*, 122–130.

Wu, J., Zeng, L., Han, B., Zhou, Y., Luo, X., Li, X., Chen, X., and Jiang, W. (2022). Analysis and design of a novel arrayed magnetic spring with high negative stiffness for low-frequency vibration isolation. *International Journal of Mechanical Sciences*, *216*, 106980.

Wu, W., Chen, X., and Shan, Y. (2014). Analysis and experiment of a vibration isolator using a novel magnetic spring with negative stiffness. *Journal of Sound and Vibration*, *333*, 2958–2970.

Xi, Z., Weili, L., Benhai, L., Jiaofen, Q., and Cheng, L. (2022). Vibration isolation effects of barriers filled with ceramsite and sand: Full-scale model test and numerical investigation. *Construction and Building Materials*, *341*, 127789.

Yilmaz, C., and Hulbert, G. (2010). Theory of phononic gaps induced by inertial amplification in finite structures. *Physics Letters A*, *374*, 3576–3584.

Yilmaz, C., and Hulbert, G. M. (2017). Dynamics of locally resonant and inertially amplified lattice materials. *Dynamics of Lattice Materials; Phani, AS, Hussein, MI, Eds*, (p. 233).

Yilmaz, C., Hulbert, G. M., and Kikuchi, N. (2007). Phononic band gaps induced by inertial amplification in periodic media. *Physical Review B*, *76*, 054309.

Yilmaz, G. (2007). Hulbert, and n. kikuchi,"phonic band gaps induced by inertial amplification in periodic media,". *Phys. Rev. B*, *76*, 054309.

Yuan, S., Sun, Y., Wang, M., Ding, J., Zhao, J., Huang, Y., Peng, Y., Xie, S., Luo, J., Pu, H. et al. (2021). Tunable negative stiffness spring using maxwell normal stress. *International Journal of Mechanical Sciences*, *193*, 106127.

Yuksel, O., and Yilmaz, C. (2015). Shape optimization of phononic band gap structures incorporating inertial amplification mechanisms. *Journal of Sound and Vibration*, *355*, 232–245.

Zhang, R., Zhao, Z., and Dai, K. (2019a). Seismic response mitigation of a wind turbine tower using a tuned parallel inerter mass system. *Engineering Structures*, *180*, 29–39.

Zhang, R., Zhao, Z., and Pan, C. (2018). Influence of mechanical layout of inerter systems on seismic mitigation of storage tanks. *Soil Dynamics and Earthquake Engineering*, *114*, 639–649.

Zhang, Z., Liu, X., and Peng, Y. (2019b). Improved nonlinear rotational constitutive law for predicting critical loads in elastomeric isolation bearings. *Construction and Building Materials*, *211*, 150–158.

Zhao, F., Ji, J., Ye, K., and Luo, Q. (2021). An innovative quasi-zero stiffness isolator with three pairs of oblique springs. *International Journal of Mechanical Sciences*, *192*, 106093.

Zhao, Z., Chen, Q., Zhang, R., Pan, C., and Jiang, Y. (2019). Optimal design of an inerter isolation system considering the soil condition. *Engineering Structures*, *196*, 109324.

Zhao, Z., Chen, Q., Zhang, R., Pan, C., and Jiang, Y. (2020a). Energy dissipation mechanism of inerter systems. *International Journal of Mechanical Sciences*, *184*, 105845.

Zhao, Z., Zhang, R., Wierschem, N. E., Jiang, Y., and Pan, C. (2020b). Displacement mitigation–oriented design and mechanism for inerter-based isolation system. *Journal of Vibration and Control*, (p. 1077546320951662).

Zheng, Y., Zhang, X., Luo, Y., Yan, B., and Ma, C. (2016). Design and experiment of a high-static–low-dynamic stiffness isolator using a negative stiffness magnetic spring. *Journal of Sound and Vibration*, *360*, 31–52.

Zhou, J., Dou, L., Wang, K., Xu, D., and Ouyang, H. (2019). A nonlinear resonator with inertial amplification for very low-frequency flexural wave attenuations in beams. *Nonlinear Dynamics*, *96*, 647–665.